LA-8671

c. 3

K-Components for the ~1.4-, ~1.6-, and ~1.7-MeV Structures in the Fission of ^{232}Th + n

University of California

LOS ALAMOS SCIENTIFIC LABORATORY
Post Office Box 1663   Los Alamos New Mexico 87545

Edited by Elaine Stanlick
Photocomposition by Marian Martinez

UNITED STATES
DEPARTMENT OF ENERGY
CONTRACT W-7405-ENG. 36

LA-8671

UC-34c
Issued: July 1981

K-Components for the ∼1.4-, ∼1.6-, and ∼1.7-MeV Structures in the Fission of ^{232}Th + n

G. F. Auchampaugh
S. Plattard*
N. W. Hill**
G. de Saussure**
R. B. Perez**
J. A. Harvey**

---

*Visiting Staff Member. Centre d'Etudes de Bruyères-le-Châtel, B. P. No. 561, 92542 Montrouge, Cedex, FRANCE.

**Oak Ridge National Laboratory, Oak Ridge, TN 37830.

K-COMPONENTS FOR THE ~1.4-, ~1.6-, AND ~1.7-MeV STRUCTURES IN THE FISSION OF ^{232}Th + n

by

G. F. Auchampaugh, S. Plattard, N. W. Hill, G. de Saussure,
R. B. Perez, and J. A. Harvey

ABSTRACT

Neutron-induced angle-integrated fission cross sections of ^{232}Th were measured from 0.7 to 9 MeV with a nominal neutron energy resolution of 0.15 ns/m. Data were taken for the angular intervals 0 to 23.4°, 0 to 33.7°, 0 to 51.7°, and 0 to 90°. The structures at ~1.4, ~1.6, and ~1.7 MeV were interpreted in terms of rotational bands with $K = 1/2$, $3/2$, and $\geq 5/2$. The approximate relative fission strengths for the K-bands are in the proportion 1.7:2.4:1.0, 0.0:2.6:1.0, and 1.0:2.8:0.0 for the three structures, respectively.

I. INTRODUCTION

The apparent "simple" structure (hereafter referred to as structure) observed in subthreshold neutron-induced fission of ^{231}Pa, ^{230}Th, and ^{232}Th is well established from high-resolution fission cross-section measurements.[1-4] The lowest energy structures occur at neutron energies of ~157, ~180, ~350, and ~370 keV in ^{232}Pa; at ~715 keV in ^{231}Th; and at ~1.4, ~1.6, and ~1.7 MeV in ^{233}Th. They have a full width at half maximum (FWHM) 2000 to 10 000 times greater than the spacing of the levels at the neutron separation energy in the first minimum of the multihumped fission barrier. In addition, they appear to be composed of many narrower structures (hereafter referred to as fine structure). Good examples of fine structure are the 157-keV structure, and possibly the 370-keV structure in ^{231}Pa. Furthermore, on a much finer energy scale, the shape of the structure or fine structure is modulated by low-amplitude structure (ultrafine structure) with a smaller spacing than appears in that of the fine structure. This is evident in the fission cross section of ^{232}Th.

Theoretical calculations, including mass asymmetric distortions, of the fission barrier for nuclei with $N \sim 142$ by Möller[5] and Möller and Nix[6] predict, in addition to the second minimum, a shallow third minimum at a much larger deformation. Because the wave functions of the states in the third minimum must be odd or even under the parity operation on the octupole deformation parameter ε_3,[5] the states occur in pairs with opposite parities. The separation between the states depends on the coupling between the two minima at $\pm\varepsilon_3$. The rotational bands built on these states have opposite parities but the same rotational constant $A = \hbar^2/2\theta$, where θ is the moment of inertia of the nucleus at the third minimum, and the same absolute value of the decoupling parameter a for the $K = 1/2$ bands; the sign of a is different for the two bands. Invoking a shallow third minimum that traps at least one vibrational state and possibly its associated rotational band can explain, at least qualitatively, the structure observed in the fission cross section in the subthreshold region.

Blons et al.[3] use the rotational model to interpret the fine structure at 715 keV in ^{231}Th in terms of the members of a K = 1/2$^-$ and a K = 1/2$^+$ band. From a shape-fitting analysis of just their fission cross-section data, they obtain 1.90 ± 0.06 keV for A and 2.28 ± 0.10 for a (both parities). When they allow the decoupling parameter to be parity dependent and use, as well, available anisotropy data, they obtain 2 keV for A, and for a, either 1.3 (K = 1/2$^+$) and −1.5 (1/2$^-$) or −1.1 (1/2$^+$) and 1.1 (1/2$^-$).[7]

Blons et al.[4] use the model to interpret the structure at 1.6 MeV in ^{233}Th in terms of two K = 3/2 bands with rotational constants of 2.46 and 2.73 keV.

It is tempting, therefore, to associate these small values for the rotational constant with the third minimum. Typical values for the ground-state deformation are about 9 keV (Ref. 8) for nuclei in this mass region. For the fission isomers that occur in the second minimum of the fission barrier, Specht et al.[9] obtain 3.33 keV for the 4-ns ^{240}Pu isomer, and Backe et al.[10] obtain 3.36 keV for the 8-µs ^{239}Pu isomer. Because the average thorium rotational constant is about 20% smaller than that for the fission isomers, a larger moment of inertia is required, consequently, the minimum occurs at a larger deformation. However, it is not clear, particularly in ^{232}Th, whether the fine structure used to deduce the rotational constant is related to the members of a K-band or to fractionation of the vibrational state into more complex configurations.[11]

A high-resolution fission cross-section measurement delineates the structure in the cross section, but the data alone do not show unequivocally that the structure belongs either to special states in the second minimum or to vibrational-mode states in the third minimum. Additional information is needed about the character of this structure, such as its angular momentum components K, J, and parity π. A measurement of the angular distribution of the fission fragments can provide information on K, J, and sometimes π. Traditionally these measurements fall into two categories: (1) differential measurements with reasonable angular resolution, but at selected energy intervals greater than the width of the fine structure and, in general, with poor resolution, or (2) integral measurements (0° to θ_m) for a few limiting angles θ_m, but at many energies over the fine structure with an energy resolution comparable to that used in the fission cross-section measurement.

In ^{231}Pa below 370 keV, where the fine-structure width is greater than 2.5 keV,[2] the differential angular distribution data[12,13] have an energy resolution $\Delta E = 2$ to 40 keV. For the 715-keV structure in ^{231}Th where the fine-structure theoretical width is about 7 keV,[3] the differential angular distribution data[14,15] have $\Delta E = 10$ to 36 keV. The time-of-flight (TOF) data* at 55 and 80° have $\Delta E < 10$ keV at 715 keV. In ^{233}Th, where the structures have a width of about 70 keV, and the fine structure has a width probably less than 10 keV, the differential angular distribution data[16,17] have $\Delta E = 50$ to 100 keV. And finally, the TOF integral angular distribution data[4] for $\theta_m = 45°$ have $\Delta E = 2.3$ keV at 1.6 MeV.

Therefore, in all differential angular distribution measurements, with few possible exceptions (Veeser and Muir, and Ref. 12), the neutron energy resolution is much greater than the width of the fine structure. The TOF measurements have the necessary energy resolution, but because the structure is more complex than at first thought, a measurement of the anisotropy at one angle, or for a rather large angular interval, does not provide sufficient information to determine K, J, and π. However, such data on even-odd transition nuclei do provide information on the relative strengths of the K = 1/2 vs K > 1/2 components in the cross section because there are significant differences between these two angular distributions: K = 1/2 distributions are peaked in the fore-aft direction relative to the beam direction whereas the K > 1/2 distributions are peaked more at 90° to the beam direction.

For differential measurements that use monoenergetic neutrons from a charged-particle reaction, a further complication that arises is knowing accurately the energy of the neutron from the reaction. An error of 5 keV, which is not unrealistic for such reactions, becomes important when trying to measure the angular distribution for a fine structure with a width of just a few kilovolts, or when comparing differential and fission cross-section data taken with different experimental conditions.

What is needed, therefore, is a high-energy resolution, good angular resolution, differential fission cross-section measurement. Such a measurement is virtually impossible with today's neutron intensities. However, as a compromise, we have undertaken anisotropy measurements of these isotopes at *more* than one limiting angle using the TOF technique. This report describes the ^{232}Th measurement.

---

*Information provided by L. R. Veeser and D. W. Muir, 1976.

II. EXPERIMENTAL DETAILS

A. General

The neutron-induced fission cross section and fission-fragment anisotropy measurements for ^{232}Th were performed at the Oak Ridge National Laboratory Electron Linear Accelerator (ORELA) using the standard water-cooled tantalum target for neutron production. The data were taken using the TOF technique with a nominal time resolution of 0.15 ns/m. The accelerator was operated at either a pulse width of 5 ns (total data acquisition time of ~343 h) or a pulse width of 6 ns (~190 h) at a repetition rate of 800 Hz and an average power on target of 8.5 kW.

B. Fission Detector

The fission-fragment detector, located at an average distance of 41.68 m from the neutron source, consists of a six-cell sealed gas scintillator filled with a 98% He, 2% N_2 mixture at STP. The chamber is pumped for several days to a pressure of less than 10^{-7} torr before it is filled with the gas mixture. The gas is not circulated and filtered during the measurement. The fission-fragment pulse-height distribution recorded simultaneously with the time information shows no pulse-height resolution degradation because of impurity build-up in the gas or breakdown of the molecules from alpha-particle radiation (over a period of several months).

Five of the cells contain natural thorium and one cell contains enriched uranium (93% ^{235}U), which is used to measure the neutron spectrum. Thorium oxide is painted to an areal density of 2 mg/cm^2 of ^{232}Th on both sides of a semicircular foil of titanium, 20 cm in diameter and 12.5 μm thick, that is sandwiched between two 20-cm-i.d., 0.5-mm-thick titanium rings. The uranium is electroplated on both sides of a 50-μm-thick stainless steel foil to an areal density of 0.5 mg/cm^2. Each foil is placed in the center of a cell that is optically isolated from the others by aluminum reflectors on all sides of the cell. A schematic diagram of the chamber is shown in Fig. 1. Cell 3 contains the uranium foil, and cells 4, 5, and 6 contain Duralumin grids placed over the fissionable deposits. Hexagonally packed holes machined into these grids limit the maximum angle θ_m of emission of the fission fragments with respect to the beam direction. The dimensional characteristics of the grids are given in Fig. 2.

Each cell is viewed by two XP 2020 Q, 5-cm-diam photomultiplier tubes manufactured by La Radiotechnique Compelec. The tubes are supplied with quartz flat-face plates. The cell windows are made of quartz to achieve the maximum possible ultraviolet transmission from the scintillating gas to the photocathode surface of the tube. The tube is mounted in direct contact with the window and held in place by springs between the tube base assembly and the chamber.

C. Electronics

A schematic showing the electronics for a pair of tubes is shown in Fig. 3. The stop signal for the EG&G TDC-100 time digitizer (TDC) is derived from a quadruple coincidence between a signal from an ORTEC 934 constant fraction discriminator (CFD) that is used for time information, signals from each of the tubes, and a signal from another CFD that is used for the fission-fragment energy bias. The range on the TDC is adjusted to cover the neutron energy region of interest and to exclude the time region of the gamma burst. The pretrigger (PT), counted down by 1000, provides a gate to enable storage of the gamma burst every 1000th beam pulse. However, during these measurements, the PT/1000 feature was disabled. The zero flight-time channel for each cell is obtained by disconnecting all stop signals to the encoder except the one corresponding to the cell being checked, and increasing the range to allow storage of the gamma burst. Also, in this way, the time drift in the electronics for each cell is periodically monitored during the measurement. This drift varied by less than a few hundred picoseconds over a period of months.

III. DATA REDUCTION

A. General

The TOF spectrum and fission-fragment pulse-height spectra for selected TOF windows were stored individually for each cell in a SEL 810B computer. The data were dumped to magnetic tape and the computer memory was cleared daily. In this way, we could monitor conveniently the time drift and time and pulse-height resolution of the detector. The 5-ns burst-width data were recorded with a time/channel of 1 ns, and the 6-ns burst-width data with a time/channel of 2 ns. Because the resolution of the fine structure in the 1-ns data did

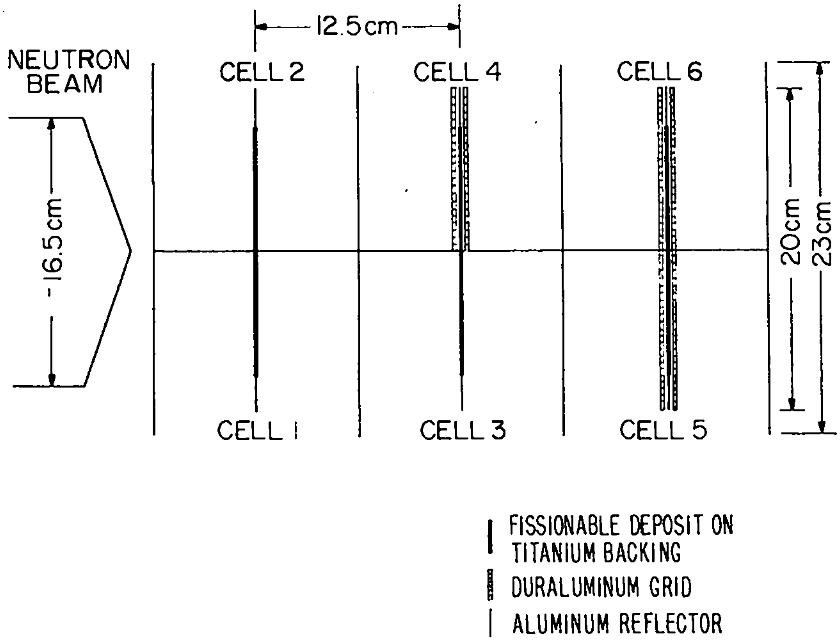

Fig. 1.
Six-cell gas scintillator detector used in the neutron-induced fission cross section and anisotropy measurements of ^{232}Th.

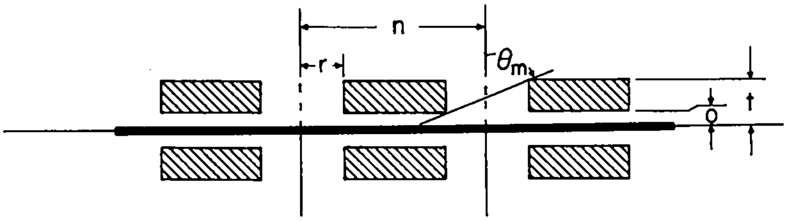

GRID CHARACTERISTICS FOR HEXAGONALLY PACKED HOLES

CELL (REFERENCED AS)	θ_m	r (mm)	n (mm)	o (mm)	t (mm)
4 (20°)	23.4	0.65	1.5	0.5	3.5
5 (30°)	33.7	1.00	2.2	0.5	3.5
6 (45°)	51.7	1.25	2.7	0.5	2.5

Fig. 2.
Dimensional characteristics of the grids in the detector.

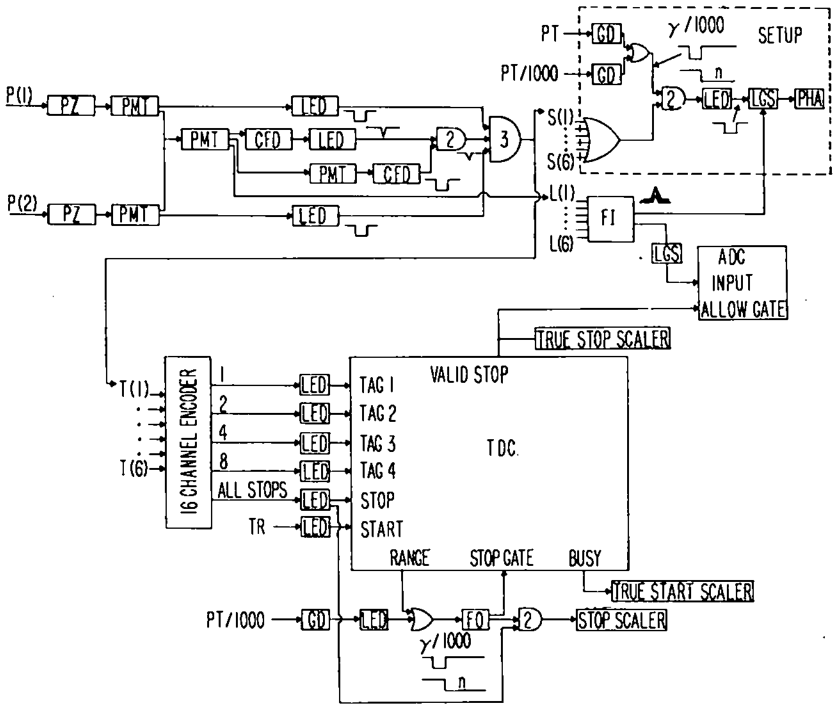

DEFINITIONS

ADC	ANALOG TO DIGITAL CONVERTER	LGS	LINEAR GATE AND STRETCHER	PZ	DIFF. WITH POLE-ZERO
CFD	CONSTANT FRACTION DISCRIMINATOR	L(i)	ith CELL LINEAR SIGNAL	S(i)	ith CELL STOP SIGNAL
FI	FAN IN	PHA	MULTICHANNEL ANALYZER	TDC	TIME TO DIGITAL CONVERTER
FILTER	40 ns NOWLIN FILTER	P(i)	ith PHOTOMULTIPLIER TUBE	T(i)	ith CELL TAG SIGNAL
FO	FAN OUT	PMT	PHOTOMULTIPLIER FO, GAINX2	TR	MACHINE TRIGGER
GD	GATE AND DELAY	PT	PRE MACHINE TRIGGER	ⓘ▷	ith - FOLD MAJORITY
LED	LEADING EDGE DISCRIMINATOR	PT/1000	PRE MACHINE TRIGGER/1000	▷	OR UNIT

Fig. 3.
Electronics for a pair of photomultipliers used for each cell.

not improve perceptibly over that of the 2-ns data, the 1-ns data were summed by 2 channels and added to the 2-ns data. The data from cells 1 and 2 were combined to form a single ungridded data set. All thorium data were corrected for deadtime and for a small time-independent background determined from the data in the region below the fission threshold, where essentially no neutron-induced fission events were expected. The uranium background was obtained at low energy where σ_f is known. The ^{235}U data were repeatedly smoothed with a third-degree seven-point smoothing polynomial before forming ratios of the individual thorium data sets to the uranium data set. And finally, the ratios were converted to cross sections using the ENDF/B-IV evaluation for the ^{235}U fission cross section. A correction was included for the contribution of ^{238}U (7%) to the ^{235}U-cell data.

B. Normalization

The ^{232}Th fission cross section at the neutron energy E_n for the *ith* cell integrated over the deposit-grid geometry (the *ith* integral fission cross section) is given by

$$\sigma_f^{232}(E_n,i) \equiv \int \frac{d\sigma_f^{232}(E_n)}{d\Omega}\, d\Omega(i)$$

$$= \frac{C_i^{232}(E_n)}{C^{235}(E_n)}\, A_i\, \sigma_f^{235}(E_n) \ , \qquad (1)$$

where i = 20, 30, 45, and 90° (Fig. 2); C_i^{232} and C^{235} refer to the net counts/channel recorded for the *ith* ^{232}Th cell and ^{235}U cell; and A_i is a normalization constant that is related to the efficiencies for detection of fission fragments and to the sample masses in the thorium and uranium cells. By choosing an energy region where the angular dependence of the fission cross section f(α) and the quantity $\sigma_f^{232}/\sigma_f^{235}$ are known, the normalization constant can be determined experimentally using the relation

$$A_1 = \frac{\sigma_f^{232}}{\sigma_f^{235}} \frac{\sum C^{235}}{\sum C_1^{232}} \frac{W_t(i)}{2\pi} , \tag{2}$$

where the sum extends over all channels in the energy region, and $W_t(i) = \int f(\alpha) d\Omega(i)$.

The best measurement of $\sigma_f^{232}/\sigma_f^{235}$ is that of Behrens,[18] who obtained an average value of 0.127 ± 0.003 for the energy interval from 3 to 5 MeV. Lo Nigro et al.[19] measured the angular dependence of the fission cross section at selected energies from 1.78 to 5.23 MeV. For the energy region from 3 to 5 MeV, f(α) can be approximated by the even-order polynomial $0.932 + 0.205 \cos^2 \alpha$. The calculated values of the $W_t(i)$ using the techniques described in Sec. III.E are $W_t(20°) = 0.109$, $W_t(30°) = 0.260$, $W_t(45°) = 0.701$, and $W_t(90°) = 2\pi$.

C. Sample Thickness Effects

The average range of a fission fragment in a thorium dioxide deposit is ~7.5 mg/cm².[20] Because the thorium deposit is rather thick (2 mg/cm², which represents a large fraction of the average range), the average maximum angle of emission of fragments from the deposit is ~82°. In the normalization of data, this affects primarily the accuracy of the cross section for the ungridded data at energies other than in the normalization region, and only if the cross section is anisotropic. This can be seen by considering the correction to the cross section at an energy E, which is given approximately by $\int f_n(\alpha) d\Omega / \int f(\alpha,E) d\Omega$. The limits on α are from 0 to ~82°; f(α,E) is the anisotropy of the cross section at E; $f_n(\alpha)$ is the anisotropy of the cross section in the normalization region. At E, this ratio is 1 if f(α,E) is isotropic, <1 if f(α,E) is peaked more fore-aft than in the normalization region, and >1 if f(α,E) is peaked more at 90°.

We have ignored this correction because it depends on knowing the anisotropy of the cross section as a function of E, which is what we are trying to measure, and it affects primarily the fission cross section for which there are several high-quality measurements. However, this effect should be kept in mind when comparing our fission cross section with those measured using thinner deposits.

D. $f^{KJ}(\alpha)$ Functions

If we assume that the fission fragments are emitted along the axis of symmetry of the nucleus, and that K is a good quantum number from the transition state to scission, then the directional dependence of the fragments is determined uniquely by the quantum numbers J, K, and M (the projection of J onto the space-fixed axis, normally taken to be the direction of the incoming projectile). The probability that a transition state defined by J, K, M emits a fragment at an angle α relative to the beam direction into a conical volume defined by the angular increment dα is given by[21]

$$dP^{KJM}(\alpha) = \frac{2J+1}{4\pi} \left| d_{MK}^{J}(\alpha) \right|^2 d\Omega , \tag{3}$$

where $d_{MK}^{J}(\alpha)$ is the absolute value of the angular part of the wave function of the Hamiltonian for a rigid rotor and is defined by the relation[22]

$$d_{MK}^{J}(\alpha) = \left\{ (J+M)!(J-M)!(J+K)!(J-K)! \right\}^{1/2}$$
$$\times \sum_n \frac{(-1)^n [\sin(\alpha/2)]^{K-M+2n} [\cos(\alpha/2)]^{2J-K+M-2n}}{(J-K-n)!(J+M-n)!(n+K-M)!n!} , \tag{4}$$

The sum is over n = 0, 1, 2 ... and contains all terms for which no negative values of the factorials occur in the denominator of the sum. The angular distribution of the fission fragments is given by $dP^{KJM}/d\Omega$ and is normalized so that

$$\int_0^\pi \frac{2J+1}{2} \left| d_{MK}^{J}(\alpha) \right|^2 \sin \alpha \, d\alpha = 1 .$$

In general, both ±K projections contribute equally to the distribution. In addition, for unaligned nuclei and for even targets, all projections of M carry equal weights. Therefore, the distribution must be averaged over ±K and summed over all allowed values of M:

$$\frac{1}{2} \sum_{M=-m_0}^{m_0} \frac{dP}{d\Omega}^{KJM}(\alpha) + \frac{dP}{d\Omega}^{-KJM}(\alpha) =$$

$$\frac{2J+1}{8\pi} \sum_{M=-m_0}^{m_0} \left| d_{MK}^{J}(\alpha) \right|^2 + \left| d_{M-K}^{J}(\alpha) \right|^2 , \tag{5}$$

where m_0 is the minimum value of $(J,I + 1/2)$ and I is the target spin.

For an even target $m_0 = 1/2$, Eq. (5) can be simplified to

$$\frac{2J + 1}{4\pi} \left[|d^J_{1/2,K}(\alpha)|^2 + |d^J_{1/2,-K}(\alpha)|^2 \right] \qquad (6)$$

using the symmetry relations[23]

$$|d^J_{MK}|^2 = |d^J_{-M-K}|^2 \quad \text{and} \quad |d^J_{M-K}|^2 = |d^J_{-MK}|^2 .$$

And finally, multiplying Eq. (6) by 2π we arrive at the expression for the f-function

$$f^{KJ}(\alpha) = \frac{2J + 1}{2} \left[|d^J_{1/2,K}(\alpha)|^2 + |d^J_{1/2,-K}(\alpha)|^2 \right] . \qquad (7)$$

To reduce our data to cross sections and to calculate theoretical cross sections for a specific K,J, we need to evaluate efficiently integrals of $f^{KJ}(\alpha)$ over the geometry of the grid in the chamber. Rather than deal with the d-functions directly, we algebraically reduce Eq. (7) to a polynomial in even powers of $\mu = \cos \alpha$. The absolute value of the d-function can be written in terms of the variables u and v, where

$u = \cos^2 \alpha/2 = (1 + \cos \alpha)/2$

and

$v = \sin^2 \alpha/2 = (1 - \cos \alpha)/2$.

The sum of the square of the d-functions contains terms $u^n v^n$ and $u^n + v^n$ (n = odd). Using the relations

$$u^n v^n = \left[\frac{1 - \mu^2}{4} \right]^n$$

and

$$u^n + v^n = \frac{1}{2^{n-1}} \left[1 + \frac{n(n-1)\mu^2}{2!} + \frac{n(n-1)(n-2)(n-3)\mu^4}{4!} + \ldots \right] ,$$

Eq. (7) reduces to

$$f^{KJ}(\alpha) = c^{KJ} \sum_{n=0}^{4} a^{KJ}_n \mu^{2n} . \qquad (8)$$

Values of the coefficients a^{KJ}_n and c^{KJ} for $1/2 \leq K, J \leq 9/2$ are listed in Table I. Equation (8) is normalized so that for a plane source $\int_0^1 f(\alpha)d\mu = 1$. The range on J, and therefore K, corresponds to a range on the neutron orbital angular momentum of $0 \leq \ell \leq 4$. Values of $\ell > 4$ make a negligible contribution to the cross section in the energy region of greatest interest in ^{232}Th, namely, $E_n < 3$ MeV.

E. $W^{KJ}_t(i)$ Integrals.

These integrals depend on the angular momentum quantum numbers K,J through the functions $f^{KJ}(\alpha)$, defined in Sec. III.D, and can be written as $W^{KJ}_t(i) = \int f^{KJ}(\alpha)\, d\Omega(i)$, where $d\Omega(i)$ is the solid angle subtended by the *ith* grid for an infinitely thin source deposit. Lent[24] presents a derivation of the solid angle for a source multicollimator detector system that can be adapted to the grid problem by considering the entrance hole of the grid, nearest the source, as an infinitely thin aperture of radius r_1 at z_1 and the exit hole of the grid as the detector of radius R at $z = 0$. For generality, we assume that $r_1 \neq R$. The geometry for this problem is illustrated in Fig. 4.

The solid angle subtended by the detector at a point (ρ,ϕ,z) in the source is defined by

$$\Omega(\rho,\phi,z) = \iint \cos \alpha \; r dr\, d\theta , \qquad (9)$$

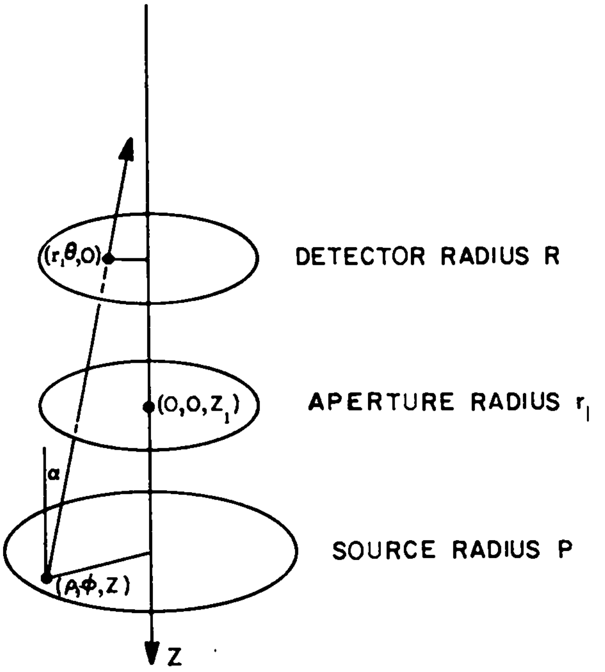

Fig. 4.
Grid geometry for the numerical calculations. The angle α defines the polar angle for a ray from the point (ρ,ϕ,z) in the source through the point $(r,\theta,0)$ in the detector.

TABLE I

VALUES FOR THE COEFFICIENTS c^{KJ} AND a_n^{KJ} IN THE EXPANSION FOR THE ANGULAR DISTRIBUTION OF THE FISSION FRAGMENTS EMITTED FROM AN EVEN-ODD TRANSITION NUCLEUS

K	J	c^{KJ}	a_0^{KJ}	a_1^{KJ}	a_2^{KJ}	a_3^{KJ}	a_4^{KJ}
1/2	1/2	1	0	0	0	0	0
1/2	3/2	1/2	1	3	0	0	0
1/2	5/2	3/4	1	−2	5	0	0
1/2	7/2	1/16	9	45	−165	175	0
1/2	9/2	5/64	9	−36	294	−644	441
3/2	3/2	3/2	1	−1	0	0	0
3/2	5/2	3/8	1	14	−15	0	0
3/2	7/2	15/16	1	−7	27	−21	0
3/2	9/2	15/32	1	20	−126	252	−147
5/2	5/2	15/8	1	−2	1	0	0
5/2	7/2	5/16	1	33	−69	35	0
5/2	9/2	35/32	1	−12	66	−100	45
7/2	7/2	35/16	1	−3	3	−1	0
7/2	9/2	35/128	1	60	−186	188	−63
9/2	9/2	315/128	1	−4	6	−4	1

where

$$\cos \alpha = \frac{z}{[z^2 + r^2 + \rho^2 - 2r\rho \cos (\theta - \phi)]^{1/2}} \; . \quad (9a)$$

If the source emits particles with an anisotropy $f^{KJ}(\alpha)$, then the weighted solid angle is given by

$$\Omega_f^{KJ}(\rho,\phi,z) = \frac{\iint f^{KJ}(\alpha) \cos \alpha \; r dr d\theta}{-\int f^{KJ}(\alpha) d(\cos \alpha)} \; . \quad (10)$$

Substituting Eq. (8) into Eq. (10) and remembering that $-\int f^{KJ}(\alpha)\, d(\cos \alpha) = 1$,

$$\Omega_f^{KJ}(\rho,\phi,z) = c^{KJ} \iint \sum_n a_n^{KJ} \cos^{2n+1} \alpha \; r dr d\theta \; . \quad (11)$$

The W(i) integral is obtained by weighting $\Omega_f(\rho,\phi,z)$ by the source distribution function $s(\rho,\phi)$, which for a circular source of radius P is given by

$$W_t^{KJ}(i) = \frac{\int_0^P \int_0^{2\pi} s(\rho,\phi) \Omega_f^{KJ}(\rho,\phi,z) \rho d\rho d\phi}{\iint s(\rho,\phi) \rho d\rho d\phi} \; . \quad (12)$$

If we assume that the source strength is uniform, then $s(\rho,\phi) = 1$ and Eq. (12) becomes

$$W_t^{KJ}(i) = \frac{1}{\pi P^2} \int_0^P \int_0^{2\pi} \Omega_f^{KJ}(\rho,\phi,z) \rho d\rho d\phi \; . \quad (13)$$

The limits on the θ and r integrals can be determined easily by projecting the aperture onto the detector plane as shown in Fig. 5. The projected area has a radius r_1' and an origin at $(d_1,\psi_1,0)$, where

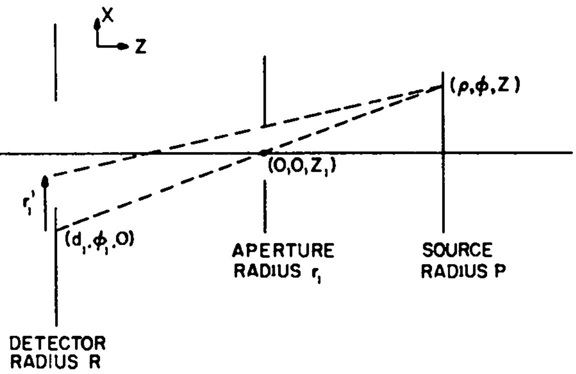

Fig. 5.

Side view of grid geometry. The dashed lines project the radius r_1 of the aperture on the detector plane from a point (ρ,ϕ,z) in the source. The projected area has an origin at $(d_1,\phi_1,0)$ in the detector plane with a radius r_1'.

$$r_1' = \frac{r_1 z}{(z - z_1)} ,$$

$$d_1 = \frac{\rho\, z_1}{(z - z_1)} ,$$

and

$$\psi_1 = \pi + \phi .$$

Diagrams of the projected areas superimposed on the detector area are shown in Fig. 6 for three possible cases: (a) $d_1 < r_1'$; (b) $r_1' < d_1 \leq \sqrt{R + r_1'^2}$; and (c) $d_1 > \sqrt{R^2 + r_1'^2}$. The limits on θ and r are those values that constrain the integration to the shaded portions in the figure. If we denote the lower and upper limits on θ and r by the subscripts L and U, respectively, then the limits on θ for the three cases are

(a) $\theta_L = 0$,

$$\theta_U = 2\pi ,$$

(b) $\theta_L = \psi_1 - \sin^{-1}\left(\frac{r_1'}{d_1}\right)$,

$$\theta_U = \psi_1 + \sin^{-1}\left(\frac{r_1'}{d_1}\right) ,$$

and

(c) $\theta_L = \psi_1 - \cos^{-1}\dfrac{(d_1^2 + R^2 - r_1'^2)}{2d_1'R}$,

$$\theta_U = \psi_1 + \cos^{-1}\frac{(d_1^2 + R^2 - r_1'^2)}{2d_1'R} , \tag{14}$$

and the limits on r for all cases are

$$r_L = \max[0, r_1^-(\theta)]$$

and

$$r_U = \min[R, r_1^+(\theta)] ,$$

where

$$r_1^-(\theta) = d_1 \cos(\psi_1 - \theta) - [r_1'^2 - d_1^2 \sin^2(\psi_1 - \theta)]^{1/2} ,$$

$$r_1^+(\theta) = d_1 \cos(\psi_1 - \theta) + [r_1'^2 - d_1^2 \sin^2(\psi_1 - \theta)]^{1/2} , \tag{15}$$

and max[,], and min[,] denote the maximum and minimum values of the variables in the brackets.

The limits $\theta_{L,U}$ and $r_{L,U}$ are a function of the grid parameters $z - z_1$, the distance between the grid and the source, z_1, the thickness of the grid, and r_1, the radius of the hole in the grid.

Lent[24] does not consider case (c), and case (b) does not reduce to case (c) for $d_1 > \sqrt{R^2 + r_1'^2}$. However, case (c) is important for distributions that are sideways-peaked, which in ^{232}Th occur for distributions with J,K > 1/2.

The complete expression for the W integral is obtained by substituting Eq. (11) into Eq. (13),

$$W_t^{KJ}(i) = \frac{c^{KJ}}{\pi P^2} \int_0^P \int_0^{2\pi} \int_{\theta_L(i)}^{\theta_U(i)} \int_{r_L(i,\theta)}^{r_U(i,\theta)} \sum_n a_n^{KJ} \cos^{2n+1}\alpha \; r\rho\, dr\, d\rho\, d\theta\, d\phi , \tag{16}$$

where $\theta_{L,U}(i)$ and $r_{L,U}(i,\theta)$ are calculated for each grid i using Eqs. (14) and (15) and cos α is given by Eq. (9a).

1. Trapezoidal Method. The multiple integral in Eq. (16) is evaluated on a CDC 7600 computer using the trapezoidal rule of numerical integration for each integral. To reduce the calculation time for a single $W_t^{KJ}(i)$, vector algorithms are used whenever possible. The efficiency of a vector operation on a 7600 computer increases with the length n of the vector because of the overhead time associated with the start-up of the vector

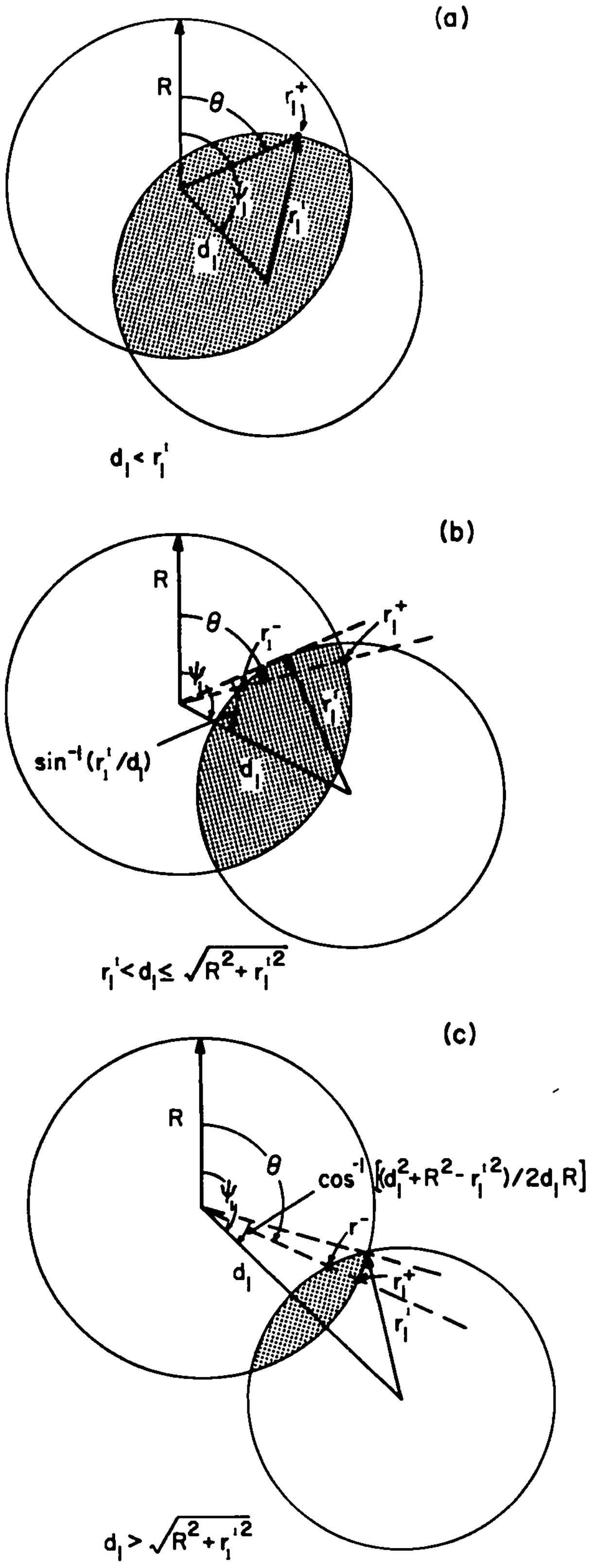

Fig. 6.

Projections of the aperture onto the detector area for the cases, (a) $d_1 < r_1'$, (b) $r_1' < d_1 \leq \sqrt{R^2 + r'^2}$, and (c) $d_1 > \sqrt{R^2 + r_1'^2}$.

operation. Therefore, it is advantageous to make n as large as possible and yet consistent with available core memory. For reasonable values of ℓ (the number of integration intervals), the improvements in run time are marginal with vectorization if each integral is evaluated separately. On the other hand, there is not enough core memory to evaluate all four integrals as one composite integral because, in this case, $n = \ell^4$. Compromising, by evaluating the radial integrals as one composite integral and with $\ell = 25$ for all integrals, we were able to calculate a $W_t^{KJ}(i)$ in about 2.5 s to an accuracy of about 10^{-3}, essentially independent of the number of terms in the expansion for $f^{KJ}(\alpha)$, at least up to 5 terms.

2. Monte Carlo Method. The multiple integral in Eq. (16) is evaluated also by using the Monte Carlo method. To achieve the same accuracy requires considerably more time, about 7 s per $W_t^{KJ}(i)$. However, the Monte Carlo method allows us to confirm the results obtained by the trapezoidal method and to investigate the effects of the adjacent six holes in the hexagonal grid pattern (Fig. 7) on the solid angle for the central hole. Because the grid does not lie on top of the deposit (Fig. 2) but is elevated from it by 0.5 mm, a fission fragment emitted from an area just below any one of the adjacent holes could pass through the central hole, thus increasing the solid angle for the central hole.

In Fig. 7, the common source area (dashed line) for hexagonal packing of circular holes is a hexagon of side length equal to $n/\sqrt{3}$, where n is the separation between the centers of the circles. To simplify the geometry for the calculation, we replace the hexagon by a circle (dash-dot line) whose area is equal to that of the hexagon. The radius of this circle is given by $r_s = (\sqrt{3}/2\pi)^{1/2}n$.

The calculations are made in two steps, one with the source centered below the central hole (W_c) and the other with the center of the source displaced by n(W_h). Therefore, the total solid angle $W_t = W_c + 6W_h$.

To illustrate the effects of the adjacent holes on $W_t(i)$, we list in Table II values of $W_c(i)$, $W_h(i)$, and $W_t(i)$ ($i =$ 20, 30, and 45°) for an isotropic distribution $f^{1/2\ 1/2}(\alpha)$, for a distribution peaked at 0°, $f^{1/2\ 5/2}(\alpha)$, and for a distribution peaked at 90°, $f^{5/2\ 5/2}(\alpha)$. We see that the effects are largest for the 45° grid and for sideways-peaked distributions.

Because the exact calculation of $W_t(i)$ is time-consuming, Eq. (16) is sometimes approximated by the integral $-2\pi \int f^{KJ}(\alpha)\, d\mu$. We have evaluated this integral for the three functions considered in Table II and list the results under the heading $W_a(i)$. The values of W_a are 3 to 5 times greater than W_t for the isotropic distribution, and 9 to 16 times greater for the sideways-peaked distribution. In fact, W_a/W_t is not the same for each grid. Therefore, any theoretical calculations of the cross section using W_a instead of W_t would not properly reproduce the trend in the data with angle, even if the calculations were normalized to a particular set of data.

Table III shows the values of $W_t^{KJ}(i)$ for the three grids and for all the functions of $f^{KJ}(\alpha)$ given in Table I.

IV. RESULTS

The ^{232}Th neutron-induced integral fission cross section in millibarns for the grid angles 20, 30, 45, and 90° are presented in Figs. 8a-d for the interval from 0.7 to 1.3 MeV, in Figs. 9a-d for the interval from 1.3 to 1.8 MeV, in Figs. 10a-d for the interval from 1.8 to 2.8 MeV, and Figs. 11a-d for the interval from 2.8 to 9 MeV. Statistical error bars are given every 10th data point. The curve through the data is obtained by applying a third-degree, five-point smoothing polynomial, six times to the data. We hope that, in this way, the true structure in the data is revealed while suppressing that from statistical fluctuations. Figures 9a-d and 10a-d have suppressed zero ordinate scales to enhance the structure in the data.

The structure observed at ~1.4 MeV, which is enhanced in the 20 and 30° data, and the structures at ~1.6 and ~1.7 MeV have received considerable attention both theoretically and experimentally. However, the structure at ~2.2 MeV, which has a peak height greater than the 1.7-MeV structure, has received very little attention. Even above this energy there are observable structures with nonnegligible peak heights. In fact at ~2.4 MeV, one structure appears as a dip in the 20 and 30° data and disappears as the grid angle is increased. This suggests a strong sideways-peaked ($K \sim J > 1/2$) component in the cross section at this energy.

In addition to the pronounced single-chance fission threshold at ~1.3 MeV, there are indications of thresholds or highly damped vibrational states at about 0.9 and 1 MeV. Also, the plateau regions show fine structure, particularly in the gridded data, that occurs at approximately the same energies in all data.

At the second-chance fission threshold at approximately 6 MeV (Figs. 11a-d), there are indications of broadened structure that persists even above the threshold, particularly apparent in the 20 and 30° data. A strong forward-peaking in the angular distribution of

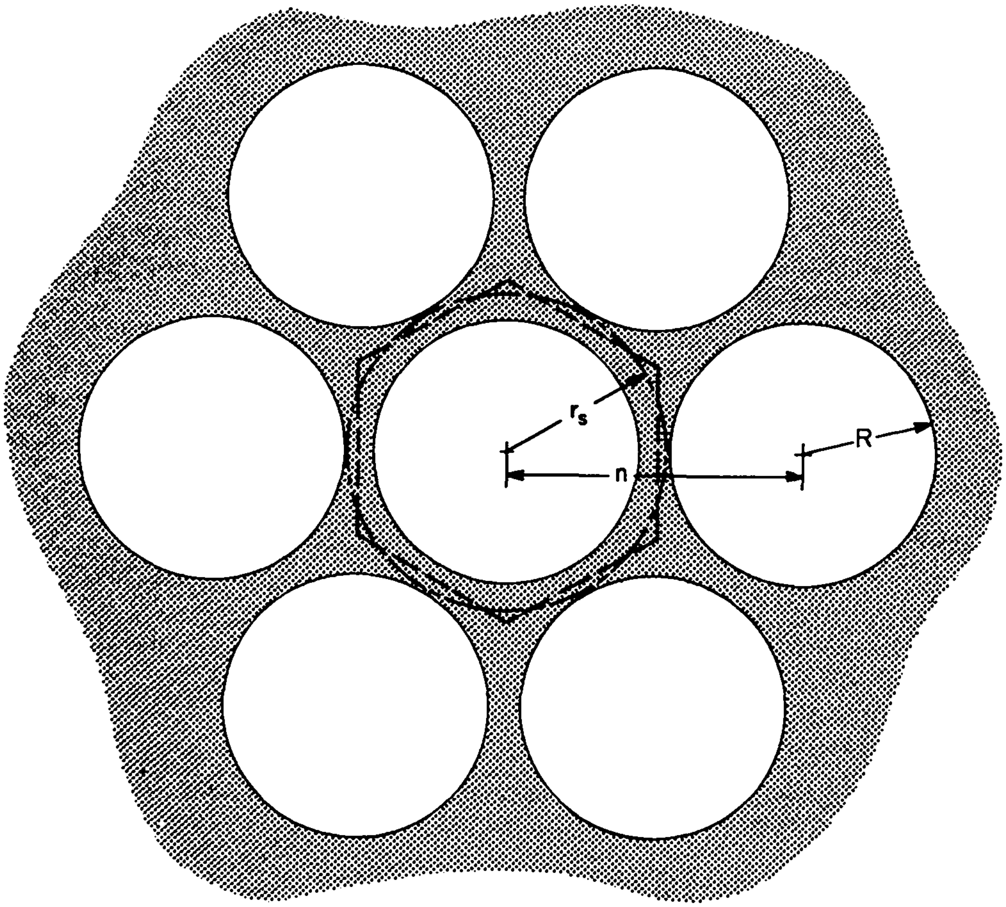

Fig. 7.
Grid pattern showing the hexagonal source area (dashed line) and the circular approximation to this area (dash-dot line). The radius of the circle $r_s = (\sqrt{3}/2\pi)^{1/2}n$.

the fission fragments has been observed in earlier measurements[25] near the second-chance threshold. Furthermore, statistical arguments about the fission process support this observation: the elastically scattered neutron in the n,n′f process leaves the transition nucleus, in this case ^{232}Th, in a rather low excited state. This state is expected to have a $K \ll J$, which would preferentially emit fragments in the fore-aft direction relative to the beam direction. However, this is the energy region, more appropriately the time region, where we can expect electronic problems associated with the intense gamma flash from the linac. And therefore, this structure may be artificial.

The smooth curve reveals low-amplitude structure throughout the entire energy region, particularly noticeable in Figs. 9a-d, which occurs at all angles and has a spacing of ~15 keV. Over the 1.6-MeV structure the energies of the low-amplitude structure peaks agree within 1 to 2 keV (our energy resolution at this energy is ~7 keV) with those observed in the recent high-resolution fission cross-section data presented by Blons et al.[7]

V. THEORETICAL CALCULATIONS

A. General

Figures 8-11 show considerable structure as well as fine structure in the data at all energies, but particularly in the 1- to 3-MeV regions. The interpretations of the structures at ~1.4, ~1.6, and ~1.7 MeV in ^{233}Th by Abou Yehia et al.,[26] Blons et al.,[4] and Caruana et al.[16] require many K-vibrational states, each with a rotational band to explain, at least qualitatively, the general features in the fission cross section. The interpretation of

TABLE II

VALUES OF $W^{KJ}(i)$ FOR AN ISOTROPIC SOURCE DISTRIBUTION, FOR A DISTRIBUTION THAT PEAKS AT 0°, AND FOR A DISTRIBUTION THAT PEAKS AT 90°

(i) (°)	$W_c(i)^{(a)}$ (sr)	$6W_h(i)^{(b)}$ (sr)	$W_t(i)^{(c)}$ (sr)	$W_a(i)^{(d)}$ (sr)
		KJ = 1/2 1/2		
20	0.092	0.004	0.096	0.517
30	0.214	0.019	0.233	1.056
45	0.549	0.085	0.634	2.355
		KJ = 1/2 5/2		
20	0.256	0.011	0.267	1.172
30	0.548	0.040	0.588	2.294
45	1.185	0.119	1.304	3.654
		KJ = 5/2 5/2		
20	0.00043	0.00008	0.00051	0.0082
30	0.0038	0.0012	0.0050	0.0655
45	0.0458	0.0222	0.0680	0.6118

[a] W_c is the value of the integral with the source centered.

[b] W_h is the value of the integral with the source displaced by n.

[c] $W_t = W_c + 6W_h$.

[d] W_a is for a distribution with no grids and with the maximum polar angle limited to θ_m (Fig. 2).

the fine structure at 715 keV in ^{231}Th by Blons et al.[3] requires two K-bands of opposite parity. Furthermore, numerical studies by Bjornholm and Lynn[11] of the coupling of pure vibrational states to intrinsic states at the deformation of the second minimum indicated that pure vibrational resonances are unlikely to occur in odd-mass nuclei; some observable degree of fractionation of the vibrational strength is to be expected; that is, the structures in the thorium isotopes, in particular for ^{233}Th, may be rather complex. For these reasons, and because the statistical quality of the gridded data is poor, any detailed theoretical analysis of our data or least-square fitting of the structures is not warranted. However, it is useful to derive values for the theoretical areas of individual K, J, π resonances and the total area for each K-band (summed over all J ≥ K components) to compare with the experimental areas. The area of a resonance with quantum numbers K, J, π for angle i is related to the area at another angle i′ by just the ratio

$$\frac{W_t^{KJ\pi}(i')}{W_t^{KJ\pi}(i)} ,$$

which is independent of the nuclear model chosen for the cross-section calculations. This is in contrast to the total K-band area, which is a sum over individual K,J^π, components with weights that do depend on the nuclear

TABLE III

VALUES OF $W_t^{KJ}(i)$ FOR i = 20, 30, AND 45°, AND FOR $1/2 \leq K, J \leq 9/2$

K	J	$W_t^{JK}(20°)$ (sr)	$W_t^{JK}(30°)$ (sr)	$W_t^{JK}(45°)$ (sr)
1/2	1/2	0.0964	0.2330	0.6340
1/2	3/2	0.1830	0.4290	1.0850
1/2	5/2	0.2670	0.5880	1.3040
1/2	7/2	0.3270	0.6760	1.3590
1/2	9/2	0.3830	0.7330	1.3730
3/2	3/2	0.0062	0.0298	0.1840
3/2	5/2	0.0225	0.1050	0.5430
3/2	7/2	0.0526	0.2140	0.8900
3/2	9/2	0.0933	0.3490	1.1010
5/2	5/2	0.0005	0.0050	0.0680
5/2	7/2	0.0029	0.0250	0.2710
5/2	9/2	0.0093	0.0710	0.5630
7/2	7/2	0.0000	0.0010	0.0280
7/2	9/2	0.0004	0.0065	0.1360
9/2	9/2	0.0000	0.0002	0.0117

model. However, this model dependence is weak, because for a particular K, the $W^{KJ}(\theta)$ functions for all $J \geq K$ (except $J = J = 1/2$) are very similar, either forward-peaked ($K = 1/2$) or sideways-peaked ($K > 1/2$).

B. Vibrational-Resonance Area

If we assume that the energy dependence of the fission cross section for a vibrational resonance located at an energy E_{vib} with quantum numbers K, J, π can be described by the Breit-Wigner function, then the area of the resonance is given by

$$A_t^{KJ\pi}(E_{vib},i) = \left(\frac{\pi}{2}\right) \sigma_f^{KJ\pi}(E_{vib},i)\Gamma_{vib}^{KJ\pi} \ ,$$

where $\sigma_f^{KJ\pi}(E_{vib},i)$ is the integral fission cross section at E_{vib} for the grid angle i, and $\Gamma_{vib}^{KJ\pi}$ is the FWHM of the resonance.

Vibrational-Resonance Width. To obtain an upper limit on the vibrational-resonance area $A_t^{KJ\pi}$, we need to choose a reasonable value for Γ_{vib}. In ^{232}Pa the resonance at 157 keV has an observed width of ~2.7 keV (our resolution <1/2 keV.[2] The structure at ~715 keV in ^{231}Th is composed of resonances with theoretical widths of ~7 keV.[3] In ^{233}Th at ~1.6 MeV, our 30° data suggest a resonance width of less than 10 keV if we assume that the structure, which has a total width of ~50 keV, is composed of several resonances. In our calculations, we use $\Gamma_{vib} = 10$ keV for all K, J, π resonances.

C. Integral Fission Cross Section

Using the Hauser-Feshbach theory[27] for compound reactions, the integral fission cross section at an energy E_n for the reaction with quantum numbers K, J, π is given by

$$\sigma_f^{KJ\pi}(E_n,i) = \frac{\sigma_{CN}^{J\pi}(E_n)\, T_f^{KJ}(E_n)\, W_t^{KJ}(i)\, S_{n,f}}{T_N^{J\pi}(E_n) + T_\gamma^{J\pi}(E_n) + T_f^{KJ}(E_n)} \ , \qquad (17)$$

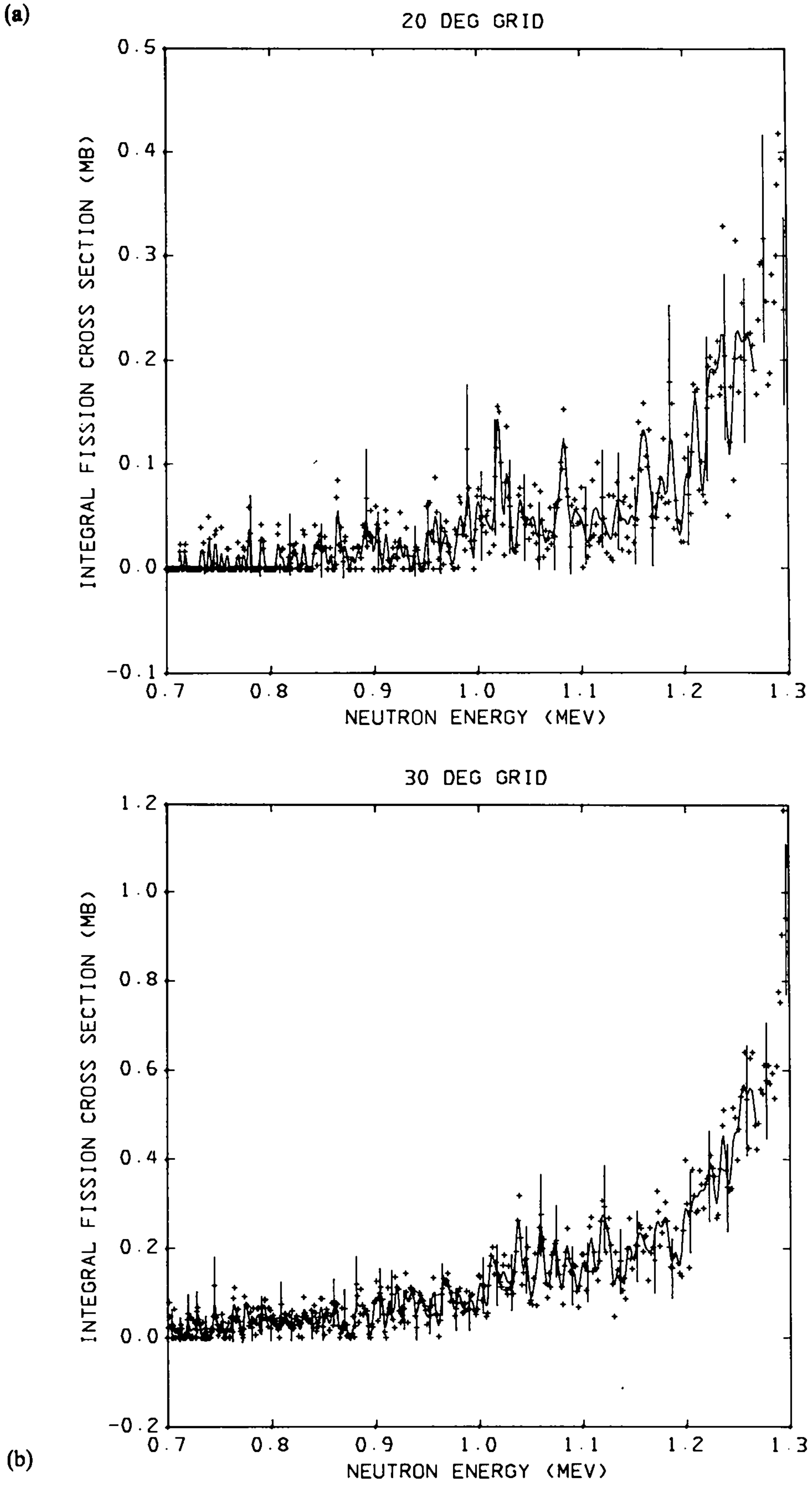

Fig. 8.
Integral fission cross sections for the energy interval 0.7 to 1.3 MeV for 20, 30, 45, and 90° grids. The solid line is obtained from smoothing the data with a five-point, third-degree polynomial applied six times.

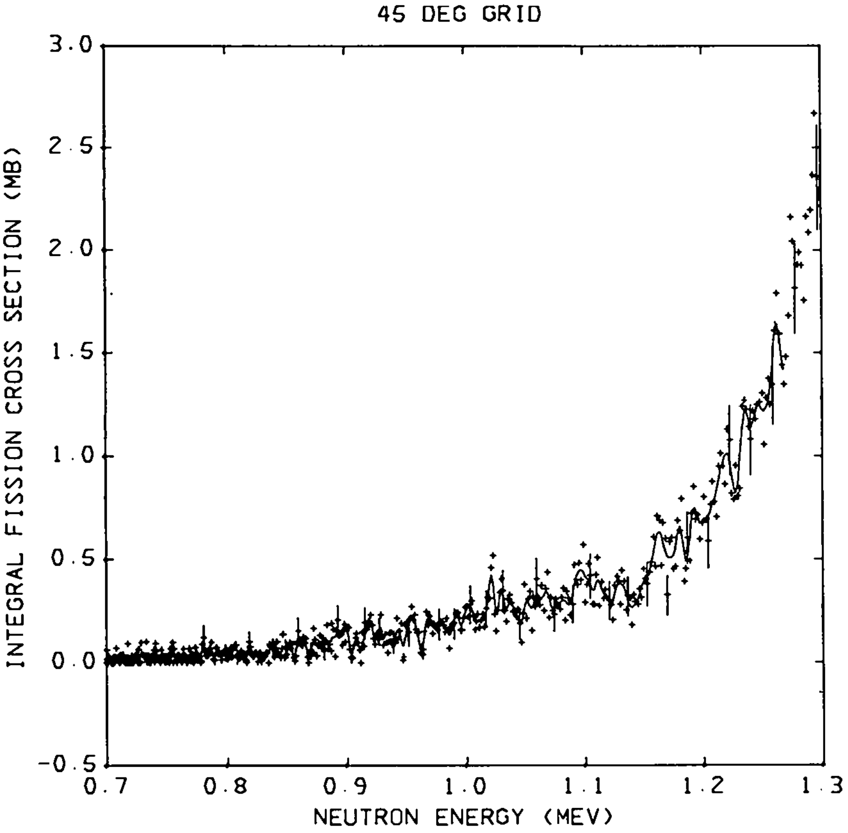
45 DEG GRID
INTEGRAL FISSION CROSS SECTION (MB)
3.0
2.5
2.0
1.5
1.0
0.5
0.0
-0.5
0.7
0.8
0.9
1.0
1.1
1.2
1.3
NEUTRON ENERGY (MEV)

(c)

(Fig. 8 cont)

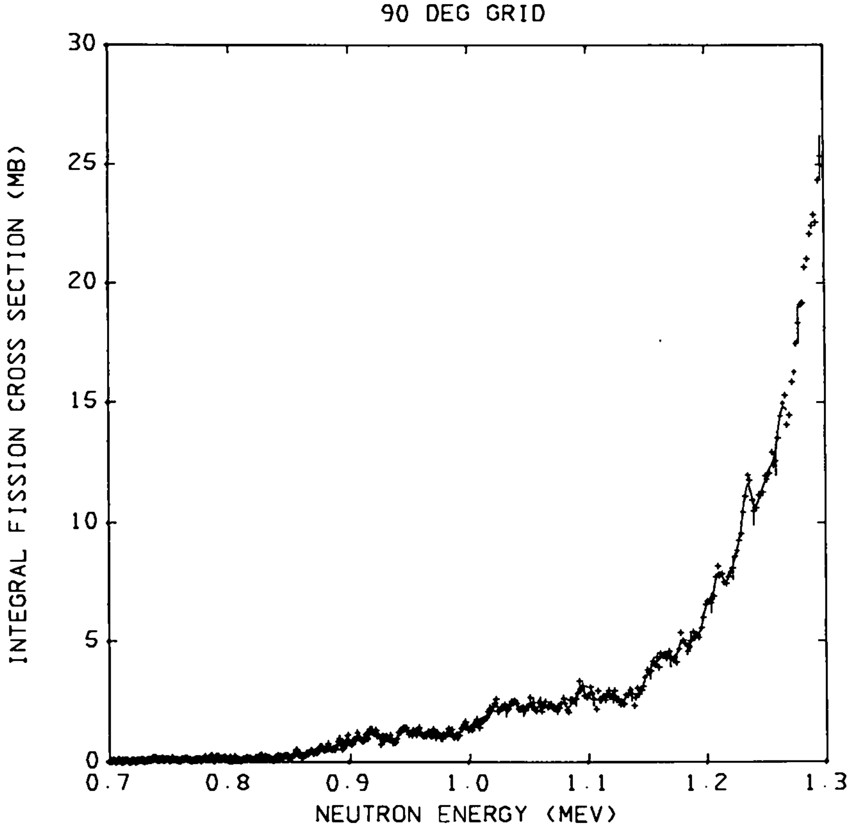
90 DEG GRID
INTEGRAL FISSION CROSS SECTION (MB)
30
25
20
15
10
5
0
0.7
0.8
0.9
1.0
1.1
1.2
1.3
NEUTRON ENERGY (MEV)

(d)

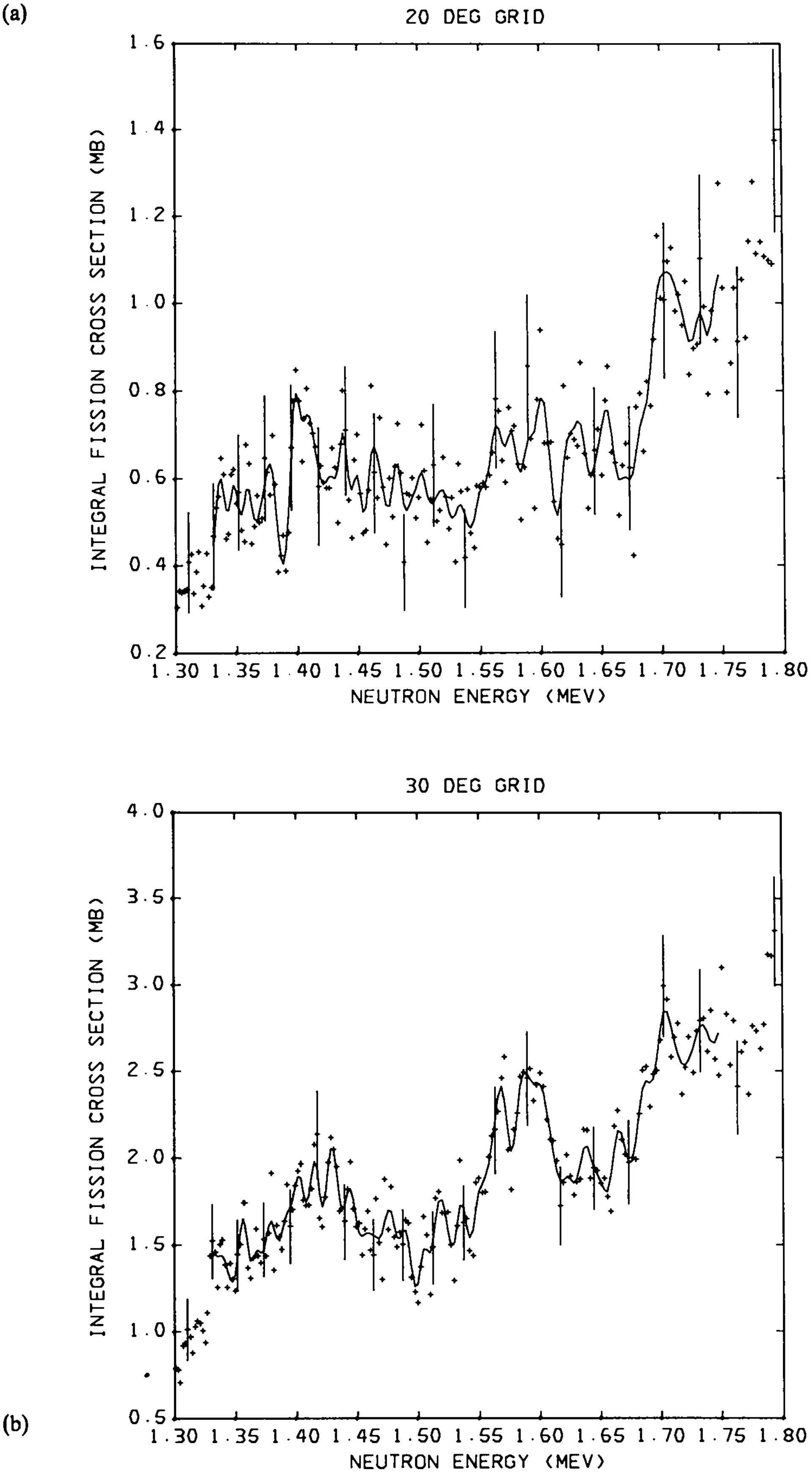

Fig. 9.
Integral fission cross sections for the energy interval 1.3 to 1.8 MeV for the 20, 30, 45 and 90° grids. The solid line is obtained from smoothing the data with a five-point, third-degree polynomial applied six times.

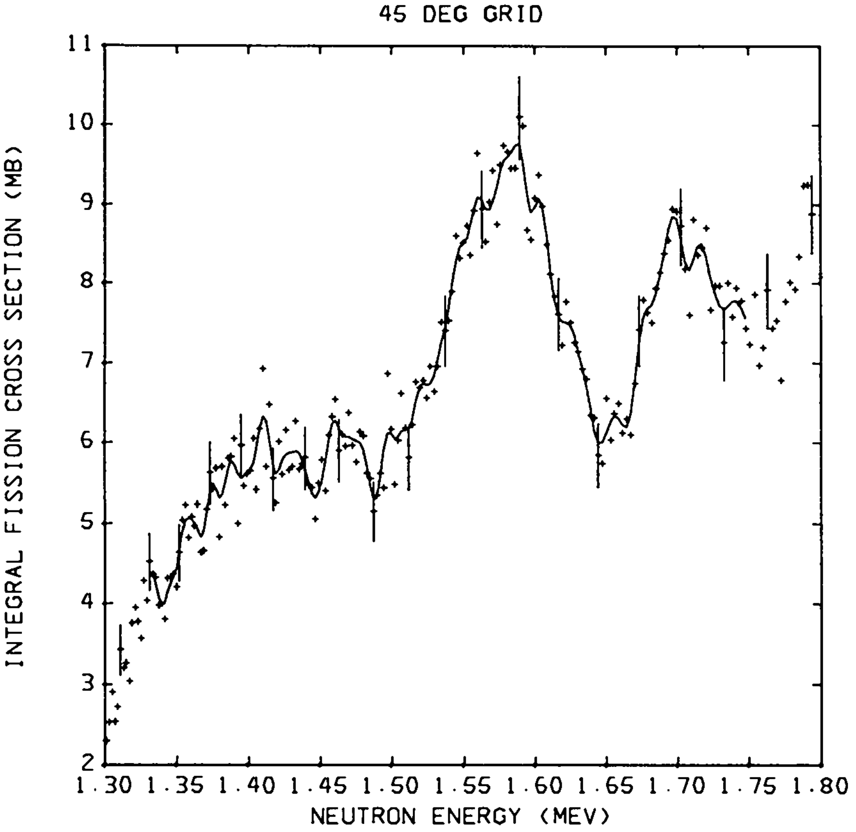
45 DEG GRID
INTEGRAL FISSION CROSS SECTION (MB)
11
10
9
8
7
6
5
4
3
2
1.30 1.35 1.40 1.45 1.50 1.55 1.60 1.65 1.70 1.75 1.80
NEUTRON ENERGY (MEV)

(c)

(Fig. 9 cont)

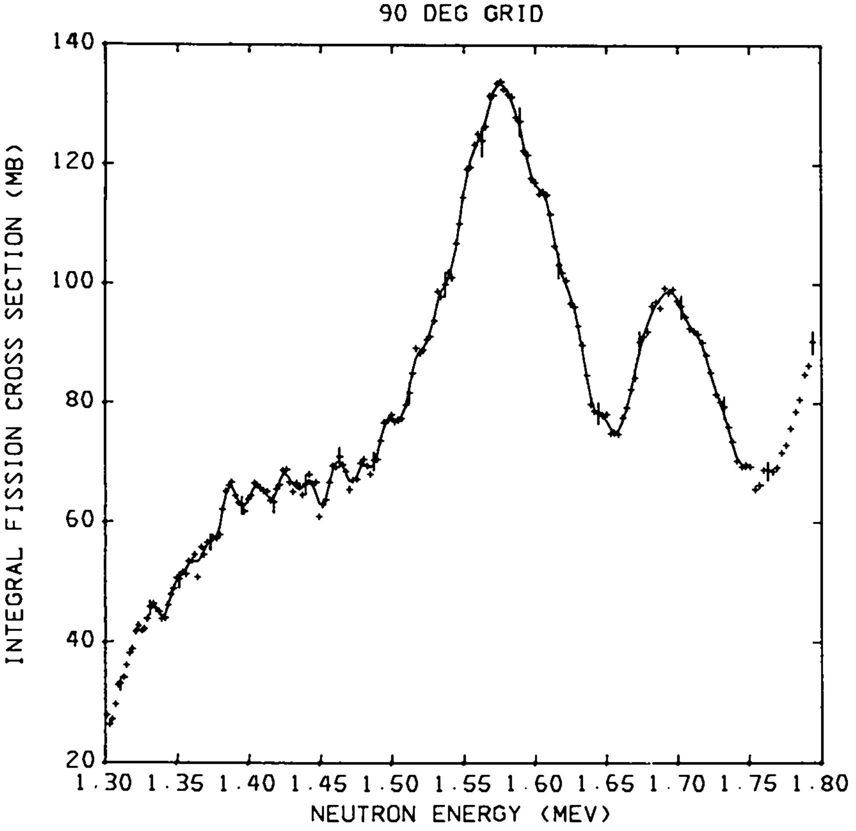
90 DEG GRID
INTEGRAL FISSION CROSS SECTION (MB)
140
120
100
80
60
40
20
1.30 1.35 1.40 1.45 1.50 1.55 1.60 1.65 1.70 1.75 1.80
NEUTRON ENERGY (MEV)

(d)

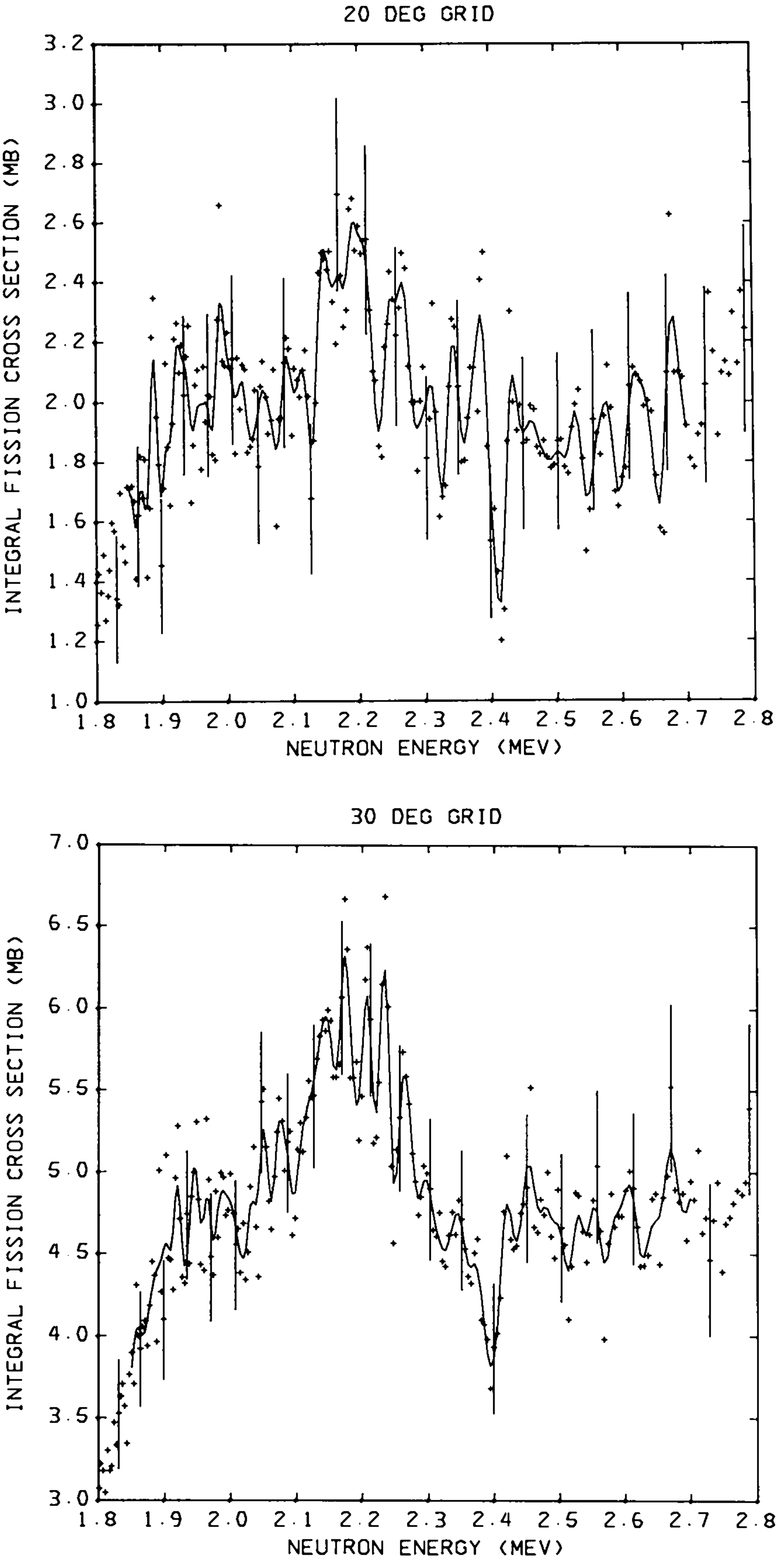

Fig. 10.

Integral fission cross sections for the energy interval 1.8 to 2.8 MeV for the 20, 30, 45, and 90° grids. The solid line is obtained from smoothing the data with a five-point, third-degree polynomial applied six times.

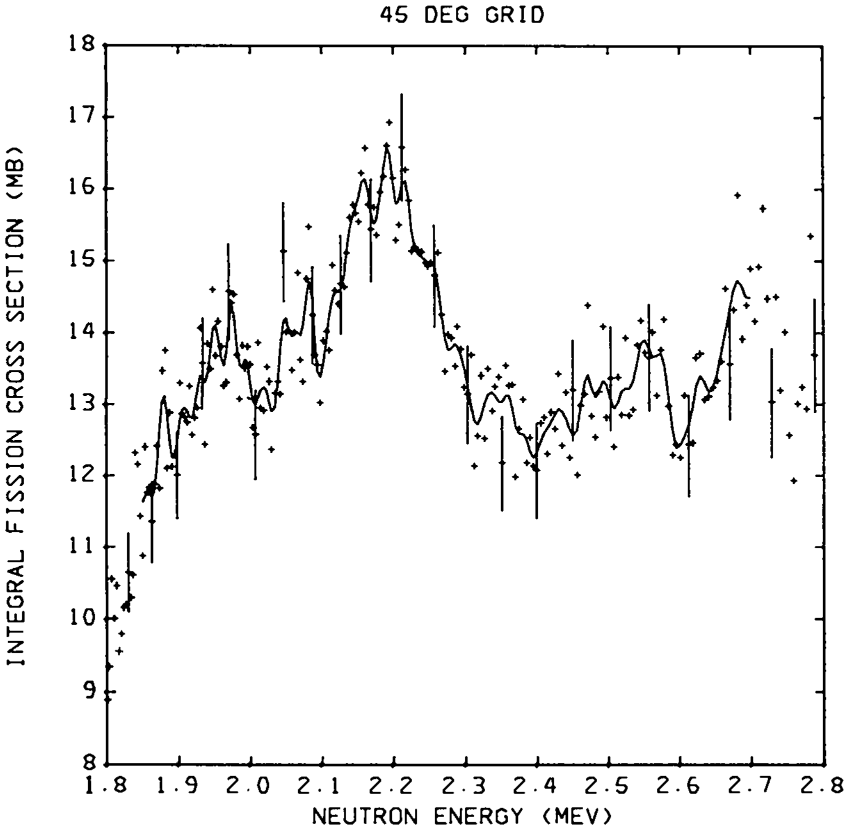

(c)

(Fig. 10 cont)

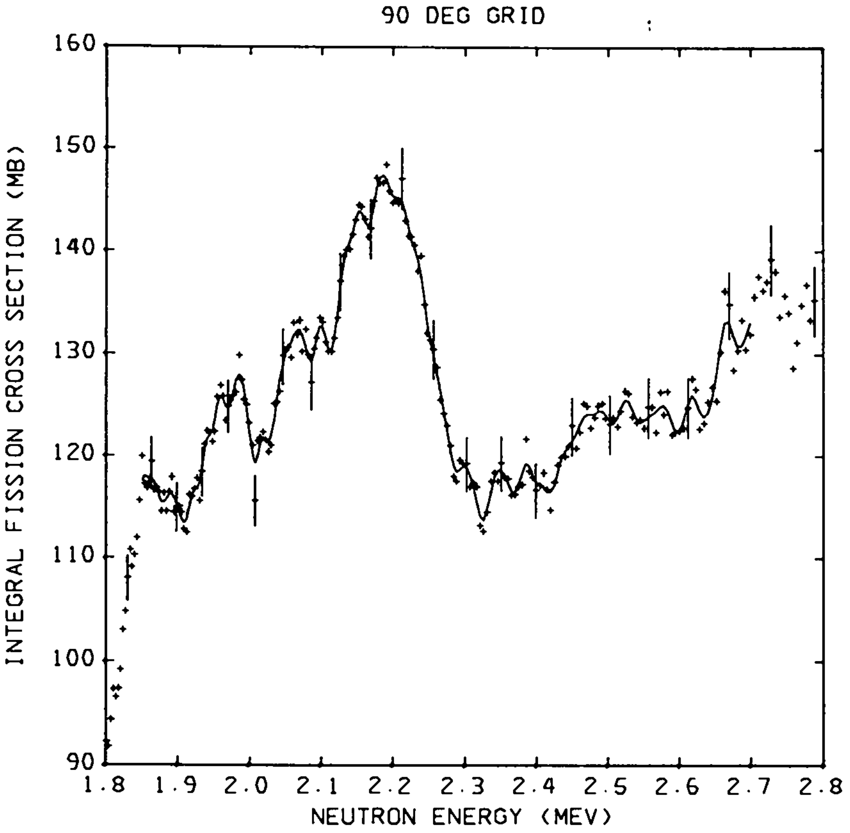

(d)

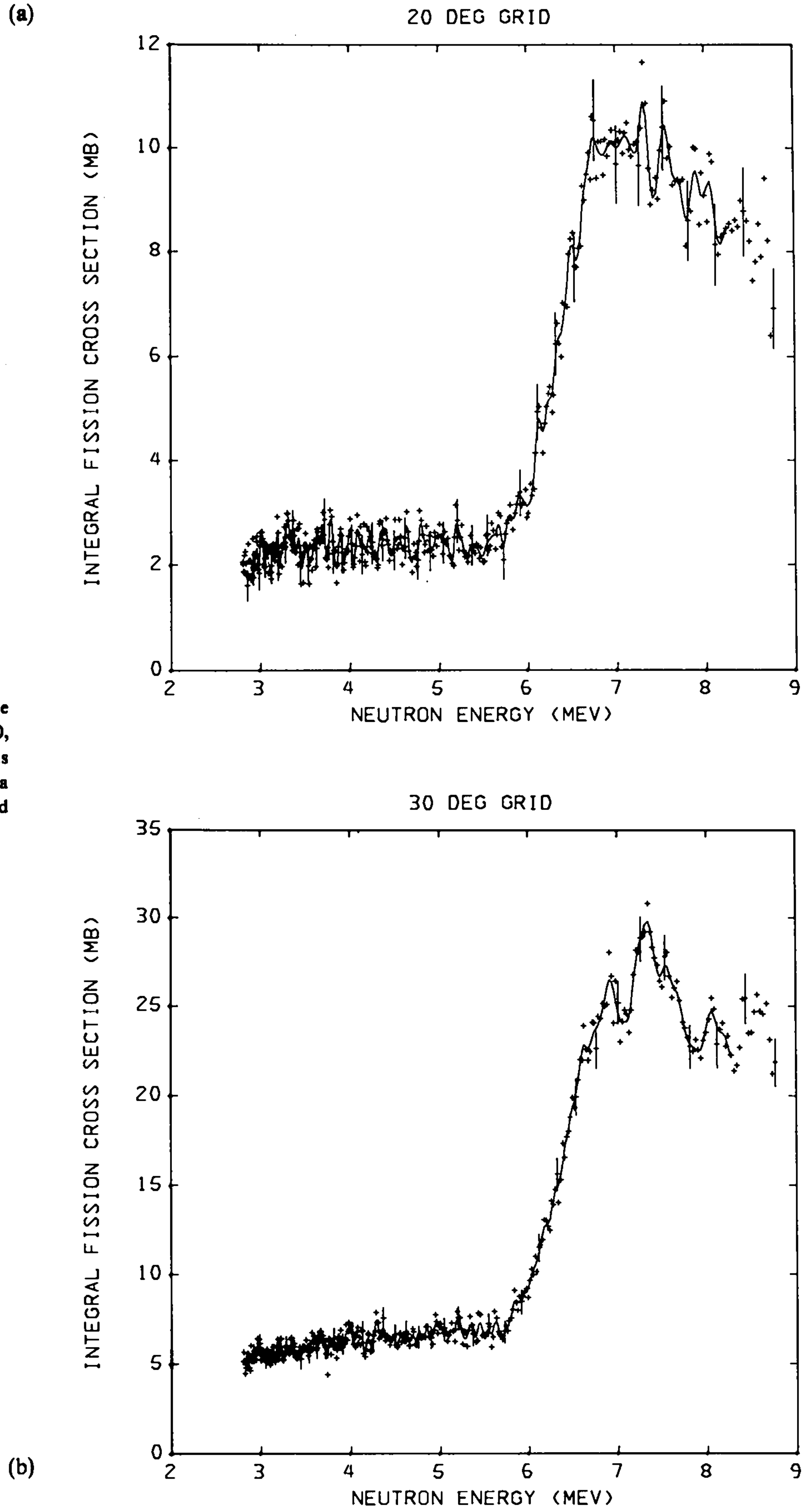

Fig. 11.
Integral fission cross sections for the energy interval 2.8 to 9 MeV for the 20, 30, 45, and 90° grids. The solid line is obtained from smoothing the data with a five-point, third-degree polynomial applied six times.

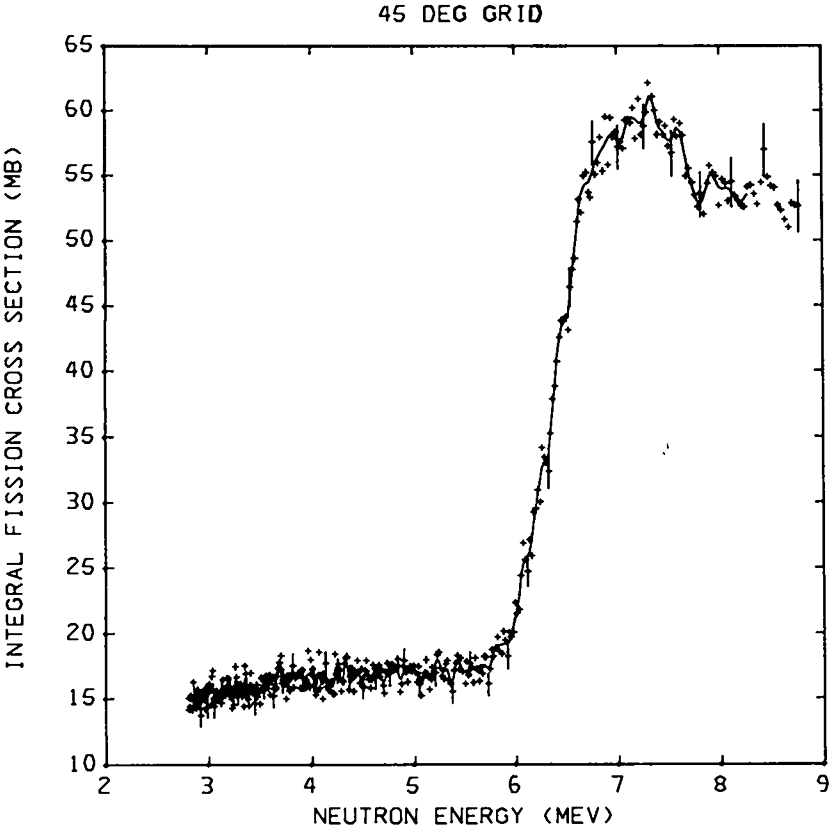

(c)

(Fig. 11 cont)

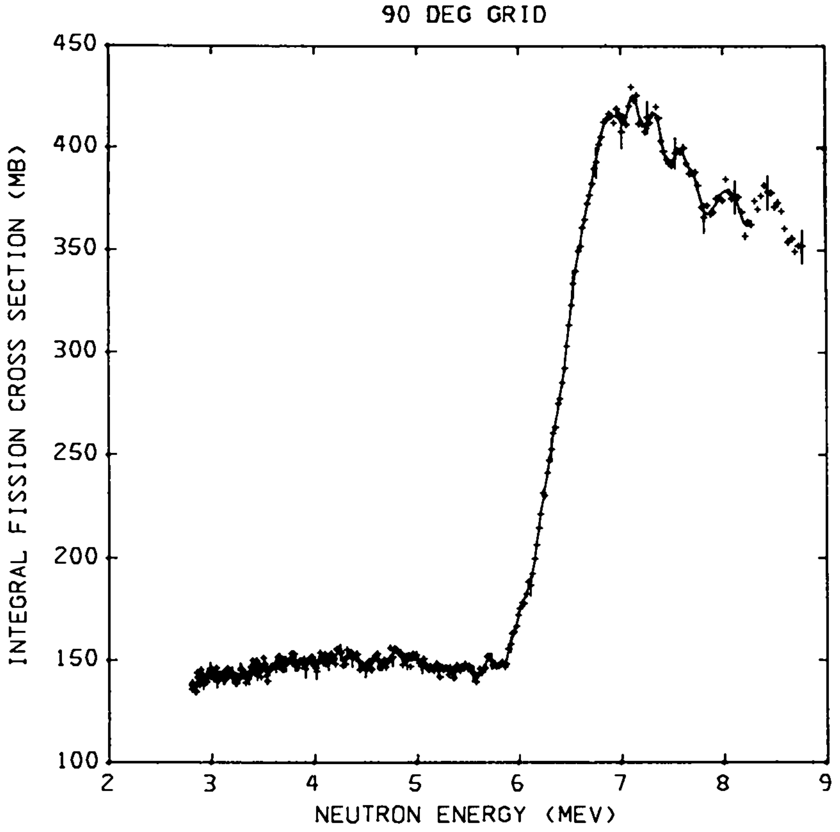

(d)

where $\sigma_{CN}^{J\pi}$ is the compound nucleus formation cross section, T_f^{KJ} is the transmission coefficient for decay through the multihumped fission barrier, $T_\gamma^{J\pi}$ is the transmission coefficient for radiative decay in the ground-state well, $T_N^{J\pi}$ is the transmission coefficient for neutron decay including elastic and inelastic scattering to states in the target nucleus, and $S_{n,f}$ is the level width-fluctuation factor, which, in the present calculations, is taken to be unity.

1. Compound-Nucleus Formation Cross Section. The compound-nucleus formation cross section in the channel-spin representation at an energy E_n can be written as

$$\sigma_{CN}^{J\pi}(E_n) = \pi \lambda_n^2(E_n)\ g(J)\ T_n^{\ell s}(E_n)\ ,$$

where $= \bar{\lambda}_n$ is the center-of-mass wavelength of a neutron of energy E_n, $g(J) = (2J + 1)/2(2I + 1)$, and $T_n^{\ell s}$ is the neutron transmission coefficient for the elastic channel with orbital angular momentum ℓ and channel spin s. The neutron transmission coefficient is related to the strength function Γ_n/D, $(\Gamma_n/D \ll 1)$ in the following way.

$$\begin{aligned} T_n^{\ell s}(E_n) &= \frac{2\pi\bar{\Gamma}_n^{\ell s}}{D} = 4\pi \left(\frac{\gamma_n^2}{D}\right)^{\ell s} P^\ell(E_n) \\ &= 4\pi S_n^{\ell s} P^\ell(E_n)\ , \end{aligned} \tag{18}$$

where $S_n^{\ell s}$ is the average reduced-strength function for the channel ℓs and P^ℓ is the neutron penetrability for neutrons of orbital angular momentum ℓ. For larger values of the strength function, a more correct expression[28,29] for $T_n^{\ell s}$ is $1 - \exp(-4\pi S_n^{\ell s} P^\ell)$. This expression has the proper limiting values, namely, $T_n^{\ell s} = 1$ for $S_n^{\ell s} \gg 1$ and $T_n^{\ell s} = 4\pi S_n^{\ell s} P^\ell$ for $S_n^{\ell s} \ll 1$. In our calculations, we use this form for $T_n^{\ell s}$ and ignore the channel-spin dependence.

Values of $\sigma_{CN}^{J\pi}(E_n)$ at $E_n = 1.6$ MeV for $1/2^\pm \leq J^\pi \leq 9/2^\pm$ are listed in Table IV. For $S_n^{\ell s}$ we use 0.019 (Ref. 30) for even values of ℓ and 0.028 (Ref. 30) for odd values of ℓ.

TABLE IV

FOR THE COMPOUND SYSTEM ^{232}Th + n, VALUES OF THE COMPOUND-NUCLEUS FORMATION CROSS SECTION $\sigma_{CN}^{J\pi}(E_n)$, FISSION CROSS SECTION $\sigma_f^{J\pi}(E_n)$ ($T_f^{KJ\pi} = 1$), RADIATIVE TRANSMISSION COEFFICIENT $T_\gamma^{J\pi}(E_n)$, AND TOTAL NEUTRON TRANSMISSION COEFFICIENT (INCLUDING ELASTIC AND INELASTIC REACTIONS) $T_N^{J\pi}(E_n)$, FOR $E_n = 1.6$ MeV

J^π	$T_N^{J\pi}$	$T_\gamma^{J\pi}$	$\sigma_{CN}^{J\pi}$ (mb)	$\sigma_f^{J\pi}$ (mb)
1/2+	6.9	0.45	199.9	23.9
3/2+	12.0	0.87	280.3	20.2
5/2+	15.4	1.22	420.5	23.9
7/2+	16.3	1.48	78.2	4.16
9/2+	17.2	1.64	97.7	4.93
1/2–	7.8	0.45	275.8	29.9
3/2–	13.8	0.87	551.7	35.2
5/2–	16.8	1.22	389.0	20.5
7/2–	18.2	1.48	518.6	25.1
9/2–	18.1	1.64	22.8	1.10

2. Radiative Transmission Coefficient. To calculate the radiative transmission coefficient, we assume that only dipole radiation contributes significantly to the radiative process. Therefore, the radiative transmission coefficient $T_\gamma^{J\pi}(E_x)$, at an excitation energy E_x in the compound system ^{233}Th, is given by

$$T_\gamma^{J\pi}(E_x) = \frac{2\pi\bar{\Gamma}\gamma}{D} = C\gamma \int_0^{E_x} \sum_{J_f=|J-1|}^{J+1} \rho^c\,(E_x - \varepsilon,\ J_f^{\pi f})\ d\varepsilon\ , \tag{19}$$

where

$\rho^c\ (E_x - \varepsilon, J_f^{\pi f})$

is the level density in the compound system at an excitation energy $E_x - \varepsilon$ for final states with total angular momentum J_f and parity π_f, and $C_\gamma = 3.63 \times 10^{-7}$. The normalization constant is determined by using for slow neutron capture ($J = 1/2^+$) in ^{232}Th the measured values 21.2 meV and 16.7 eV (Ref. 30) for $\bar{\Gamma}_\gamma$ and D, respectively.

At high excitation energy, the contribution to the nuclear level density comes from combinations of nucleons independently excited from the ground state.

This gives rise to the well-known independent particle level density relation

$$\rho(U,J^{\pi}) = \frac{(2J+1)\ \exp[-(2J+1)^2/8\sigma^2]}{4\sqrt{2\pi}\,\sigma^3} \times$$

$$\frac{\sqrt{\pi}\exp[-(2\sqrt{aU})]}{12a^{1/4}U^{5/4}}\ , \tag{20}$$

where $\sigma^2 = 0.0888\ aTA^{2/3}$, $T = \sqrt{U/a,}$ and $a = \pi^2\rho_g/6$. The single-particle level density ρ_g at the Fermi surface is given approximately by A/12.5. U is the effective excitation energy corrected for pairing effects in the nucleus using the method proposed by Gilbert and Cameron,[31] and is given by

$$U = E_x - \varepsilon - P(Z) - P(N).$$

For ^{233}Th, P(N) = 0, P(Z) = 0.78, and a = 31.6 MeV^{-1}. In the calculations of $T_{\gamma}^{J\pi}$, we use this form for the level density and allow σ to vary with energy according to the above dependence on U through the nuclear temperature T.

Values of $T_{\gamma}^{J\pi}(E_n)$ at $E = 1.6$ MeV for $1/2 \leq J \leq 9/2$ are listed in Table IV. We have assumed implicitly that, to first order, the nuclear level density is the same for both parities.

3. Total Neutron Transmission Coefficient. The total neutron transmission coefficient for elastic and inelastic scattering to states in the residual nucleus at an excitation energy E_x is given by

$$T_N^{J\pi}(E_x) = \int_0^{E_x-S_N} \sum_{I} \sum_{S=|I-1/2|}^{I+1/2} \sum_{\ell=|J-S|}^{J+S}$$

$$T_n^{\ell}(\varepsilon)\rho^R(E_x - S_N - \varepsilon,\ I^{\pi_l})d\varepsilon\ , \tag{21}$$

where

$$\rho^R(E_x - S_N - \varepsilon, I^{\pi_l})$$

is the level density in the residual nucleus at the excitation energy $E_x - S_N - \varepsilon$, I = spin of the residual nucleus with parity $\pi_l = (-1)^{\ell}\pi$, and S_N is the neutron separation energy in ^{233}Th, which is equal to 4.789 MeV.[30]

Above an excitation energy $E_x - S_N = 0.8$ MeV in the residual nucleus, ρ^R is represented by the constant-temperature level density relation $\rho^R(U) = C_n e^{-U/\theta}$, where θ is the nuclear temperature and C_n is the normalization constant that is obtained from fitting the integral distribution of known levels in ^{232}Th (Ref. 32) up to 1.6 MeV with the function

$$\frac{C_n}{2}\sum_{I=0}^{\infty}(2I+1)\ \exp-\left[\frac{(2I+1)^2}{8\sigma^2}\right] \times$$

$$\int_0^{1.6}\rho^R(U)\,dU\ .$$

The constant 1/2 implies that both parities contribute equally to the level density. For θ = 0.58 MeV and σ = 5.3 (Ref. 29), $C_n = 0.211$. Below $E_x = 0.8$ MeV, discrete levels in ^{232}Th are used to preserve the known spin and parity of these levels.

Values of $T_N^{J\pi}(E_n)$ at $E_n = 1.6$ MeV for $1/2^{\pm} \leq J\pi \leq 9/2^{\pm}$ are listed in Table IV.

4. Fission Transmission Coefficients. Calculations of fission barriers[5,6] for the protactinium and thorium isotopes show that the inner barrier is lower than the outer barrier, and furthermore, that the outer barrier is split into two barriers separated by a shallow minimum. In fact, the inner barrier height may lie below the neutron separation energy. Consequently, if we are interested only in the properties of the states trapped in this shallow well, then the effect of the inner barrier on these properties is minimal. Therefore, we can replace the triple-humped barrier by a double-humped barrier.

The energy dependence of the penetrability of transmission coefficient through a double-humped potential represented by two inverted parabolas connected smoothly to a third parabola can be calculated exactly using the wave equation[33] or approximately using the WKB method.[34]

Using the WKB approximation, the relations between the fission barrier parameters and the vibrational resonance parameters are

$$T_{f,\max}(E_{vib}) = \frac{4T_BT_C}{(T_B+T_C)^2}\ , \tag{22a}$$

$$\Gamma_{vib} = \frac{\hbar\omega_{III}}{2\pi}(T_B + T_C) \ , \qquad (22b)^*$$

$$E_{vib} = E_{III} + \hbar\omega_{III}\,(n + 1/2) \ , \ n = 0, \ 1, \ 2 \ \ldots \ , \qquad (22c)$$

and

$$T_{B.C} = \frac{1}{\left\{ 1 + \exp\left[\frac{2\pi}{\hbar\omega_{B.C}} (E_{B.C} - E_{vib}) \right] \right\}} \ , \qquad (22d)$$

where E_B, E_C are the inner and outer barrier heights, E_{III} the depth of the intermediate well, and $\hbar\omega_B$, $\hbar\omega_C$, and $\hbar\omega_{III}$ are the barrier curvatures. Therefore, six parameters are required to define uniquely $T_{f.max}$, Γ_{vib}, and E_{vib}. Measuring $T_{f.max}$ and Γ_{vib} for one structure does not determine the parameters of the barriers. Conversely, without information on the barrier parameters, $T_{f.max}$ and Γ_{vib} can be chosen independently of each other. Solving the wave equation produces similar results as long as the trapped level is well below the height of the lower barrier. To calculate a maximum resonance area, we can set $T_{f.max} = 1$.

D. Results For The Vibrational-Resonance Areas

Theoretical values of individual resonance areas $A_t^{KJ\pi}(E_n,i)$ for i = 20, 30, 45, and 90° ($\theta_m = 90°$), $1/2^{\pm} \leq$ K, $J^{\pi} \leq 9/2^{\pm}$, and $E_n = 1.6$ MeV are listed in Table V. In calculating these areas, we use the values of $\sigma_f^{KJ\pi}(T_{f.max} = 1)$ listed in Table IV and let $\Gamma_{vib} =$ 10 keV. These areas can be scaled by $T_{f.max} \times \Gamma_{vib}/10$ for other choices of Γ_{vib} and $T_{f.max}$. The areas for complete K-bands,

$$A_t^{K\pi}(E_n,i) = \sum_{J \geq K}^{J=9/2} A_t^{KJ\pi}(E_n,i) \ ,$$

are listed in Table VI.

Tables V and VI, for i = 20 and 30°, show that the most important contribution to the area of a structure in the 1- to 2-MeV region comes from K = 1/2 and K = 3/2 components. The K > 3/2 components are minimal even for i = 45° and become important only for i = 90°.

TABLE V

VALUES OF THEORETICAL VIBRATIONAL RESONANCE AREAS $A_t^{KJ\pi}(E_n,i)$ FOR i = 20, 30, 45, AND 90°, $1/2^{\pm} \leq$ K, $J^{\pi} \leq 9/2^{\pm}$, $\Gamma_{vib} = 10$ keV, AND $T_{f.max}^{KJ\pi} = 1$ AT $E_n = 1.6$ MeV

KJ$^{\pi}$		20°	30° (mb-keV)	45°	90°
1/2	1/2+	5.8	13.9	37.8	375.4
1/2	3/2+	9.2	21.7	54.8	317.3
1/2	5/2+	16.0	35.1	77.9	375.4
1/2	7/2+	3.4	7.0	14.1	65.3
1/2	9/2+	4.7	9.0	16.9	77.4
1/2	1/2−	7.2	17.4	47.3	469.7
1/2	3/2−	16.1	37.8	95.5	552.9
1/2	5/2−	13.7	30.1	66.8	322.0
1/2	7/2−	20.5	42.4	85.3	394.3
1/2	9/2−	1.1	2.0	3.8	17.3
3/2	3/2+	0.3	1.5	9.3	317.3
3/2	5/2+	1.5	6.3	32.4	375.4
3/2	7/2+	0.5	2.2	9.3	65.3
3/2	9/2+	1.1	4.3	13.6	77.4
3/2	3/2−	0.5	2.6	16.2	552.9
3/2	5/2−	1.3	5.4	27.8	322.0
3/2	7/2−	3.3	13.4	55.8	394.3
3/2	9/2−	0.3	1.0	3.0	17.3
5/2	5/2+	0.0	0.3	4.1	375.4
5/2	7/2+	0.0	0.3	2.8	65.3
5/2	9/2+	0.1	0.9	6.9	77.4
5/2	5/2−	0.0	0.3	3.5	322.0
5/2	7/2−	0.2	1.6	17.0	394.3
5/2	9/2−	0.0	0.2	1.5	17.3
7/2	7/2+	0.0	0.0	0.3	65.3
7/2	9/2+	0.0	0.1	1.7	77.4
7/2	7/2−	0.0	0.1	1.8	394.3
7/2	9/2−	0.0	0.0	0.4	17.3
9/2	9/2+	0.0	0.0	0.0	77.4
9/2	9/2−	0.0	0.0	0.0	17.3

---

*Gai et al.[34] incorrectly give the FWHM of the resonances as

$$\frac{\hbar\omega_{III}}{2\pi}\ \frac{(T_B + T_C)}{2} .$$

TABLE VI

VALUES OF THEORETICAL K-BAND AREAS $A_t^{K\pi}(E_n,i)$ FOR i = 20, 30, 45, AND 90°
$1/2^{\pm} \leq K^{\pi} \leq 9/2^{\pm}$, $\Gamma_{vIb} = 10$ keV,
AND $T_{f.max}^{KJ\pi} = 1$ AT $E_n = 1.6$ Mev

K^{π}	20°	30° (mb-keV)	45°	90°
1/2+	39.1	86.8	201.6	1210.9
3/2+	3.5	14.3	64.6	835.5
5/2+	0.2	1.4	13.8	518.2
7/2+	0.0	0.1	2.0	142.8
9/2+	0.0	0.0	0.1	77.4
1/2−	58.6	129.7	298.7	1756.2
3/2−	5.4	22.4	102.9	1286.5
5/2−	0.2	2.0	22.0	733.6
7/2−	0.0	0.1	2.1	411.5
9/2−	0.0	0.0	0.0	17.3

The gridded data (i = 20, 30, 45°) are most sensitive to the $K \leq 3/2$ components.

VI. COMPARISON OF EXPERIMENTAL AND THEORETICAL AREAS

A. General

Experimental values for the areas of the structures at 1.4, 1.6, and 1.7 MeV are plotted in Figs. 12-14 as a function of the angle θ_m (Fig. 2). The lower and upper limits are 1.33 and 1.5 MeV for the 1.4-MeV area; 1.5 and 1.65 MeV for the 1.6-MeV area; and 1.65 and 1.75 MeV for the 1.7-MeV area. These values represent the areas above a baseline drawn under the structures that approximates the plateau region above the fission threshold at ~1.3 MeV. The errors plotted are conservative estimates of how accurately we can define the areas.

The solid lines in these figures represent the trend of the theoretical areas listed in Table VI with angle for complete $K = 1/2^-$ and $K = 3/2^-$ bands. The dashed lines in Figs. 12 and 14 represent cases for combinations of a $K = 1/2^-$ band and a $K = 3/2^-$ band with the weights indicated in the figures.

We have normalized the theoretical areas to the experimental areas at $\theta_m = 33.7°$. We are allowed this freedom as long as the ratio of the experimental to theoretical areas times Γ_{vIb} does not exceed the minimum observed width of the structure. For instance, the theoretical areas for the 1.6-MeV structure could be increased by a factor of 5 [observed width of the structure in the 30° data (~50 keV) divided by the actual width used in Tables V and VI] before violating this constraint. However, not all members of a K-band could have a width of 50 keV and preserve an overall width for the band of 50 keV. It is possible that the structure is composed of several K-bands, in which case the theoretical area would be a sum over these bands, and we would not necessarily have to increase Γ_{vIb} to match the experimental areas.

In the following section, we do not explicitly specify the parity of the K-band because both parity bands give comparable results. In addition, we use the results in Tables V and VI for $E_n = 1.6$ MeV and ignore the energy dependence of these results.

B. Complete K-Band Area Results

1. 1.4-MeV Structure. For the 1.4-MeV structure, the trend in the experimental gridded areas with angle can be explained almost entirely by a $K = 1/2$ band. However, the $K = 1/2$ band underestimates the 90° area by about a factor of 2. This can be improved slightly by combining a $K = 3/2$ band with a $K = 1/2$ band in the ratio of 2:1 as shown in Fig. 12 by the dashed line. These two bands in this ratio more than account for the observed gridded areas, which means $T_{f.max}$ and/or Γ_{vIb} can be smaller. Also, if we normalize the theoretical areas for these two bands in the ratio 2:1 to the 33.7° experimental area and use the ungridded area to calculate the relative fission strengths (integrated over polar angle) for $K = 1/2$, 3/2, and $\geq 5/2$ bands, we find that they are in the proportion of 1.7:2.4:1.0. A conservative estimate of the uncertainty on these ratios is about ±15%.

2. 1.6-MeV Structure. For the 1.6-MeV structure, the gridded areas can be explained entirely by several $K = 3/2$ bands, as shown in Fig. 13 by the solid line labeled $K = 3/2$. A single $K = 3/2$ band does not have sufficient area, even if Γ_{vIb} is greater than 10 keV, to account for the experimental gridded areas. Likewise, these bands do not account for all the 90° area; in fact, they account for

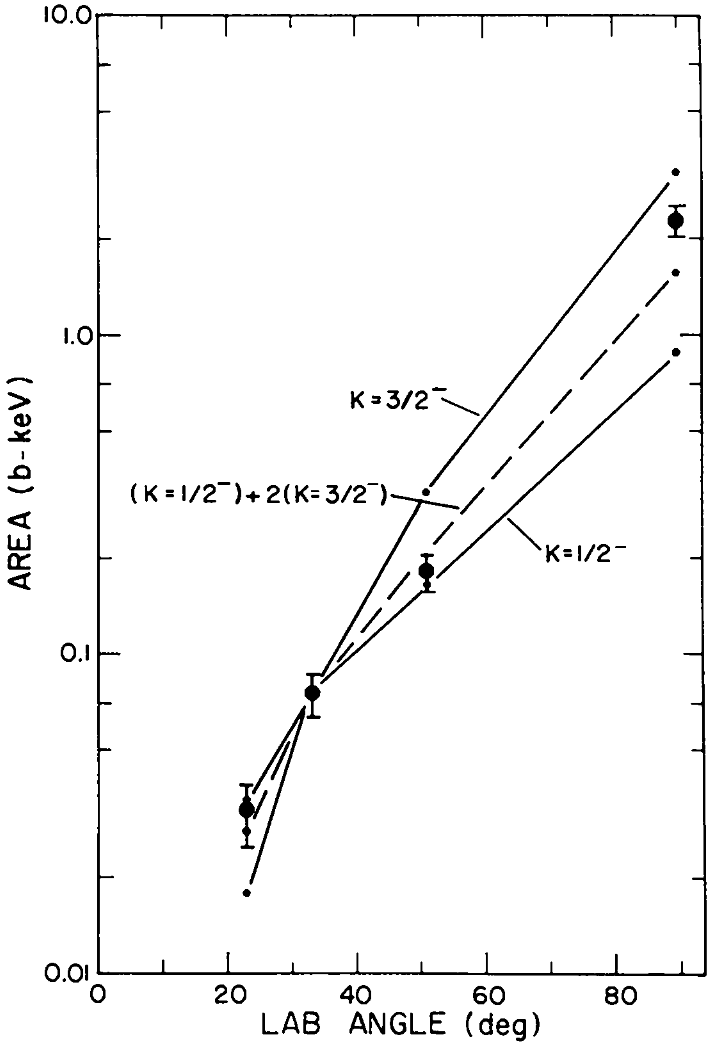

Fig. 12.
Comparison of the experimental areas with theoretical predictions of complete rotational bands for the 1.4-MeV structure. The solid lines connect the theoretical areas for a K = 1/2⁻ band and a K = 3/2⁻ band. The dashed line connects the areas for the combination (K = 1/2⁻) + 2(K = 3/2⁻). All curves are normalized to the experimental area at θ_m = 33.7°. The predictions for the positive parity bands are similar.

only about 3/4 of the area. Even if there is a significant K = 1/2 component in the 1.6-MeV structure, it would not help at 90°; $A_t^{1/2}(90°) \ll A_t^{3/2}(90°)$. Therefore, we are required again to invoke K ≥ 5/2 components in the 1.6-MeV structure. In this case, however, the unaccounted-for 90° area, about 4 b·keV, would require many K ≥ 5/2 bands because they have relatively weak strength at 90°. Assuming that most of the experimental area at 33.7° is a result of K = 3/2 bands, the approximate relative fission strengths (integrated over polar angle) for the K = 1/2, 3/2, and ≥ 5/2 bands are in the proportion of 0.0:2.6:1.0.

3. 1.7-MeV Structure. For the 1.7-MeV structure, neither a K = 1/2 nor a K = 3/2 band separately accounts for the gridded areas. However, if we combine these bands in the ratio of 4(K = 3/2):/(K = 1/2), then we can fit rather well all experimental areas, even the 90° area, as indicated by the dashed line in Fig. 14. The sum

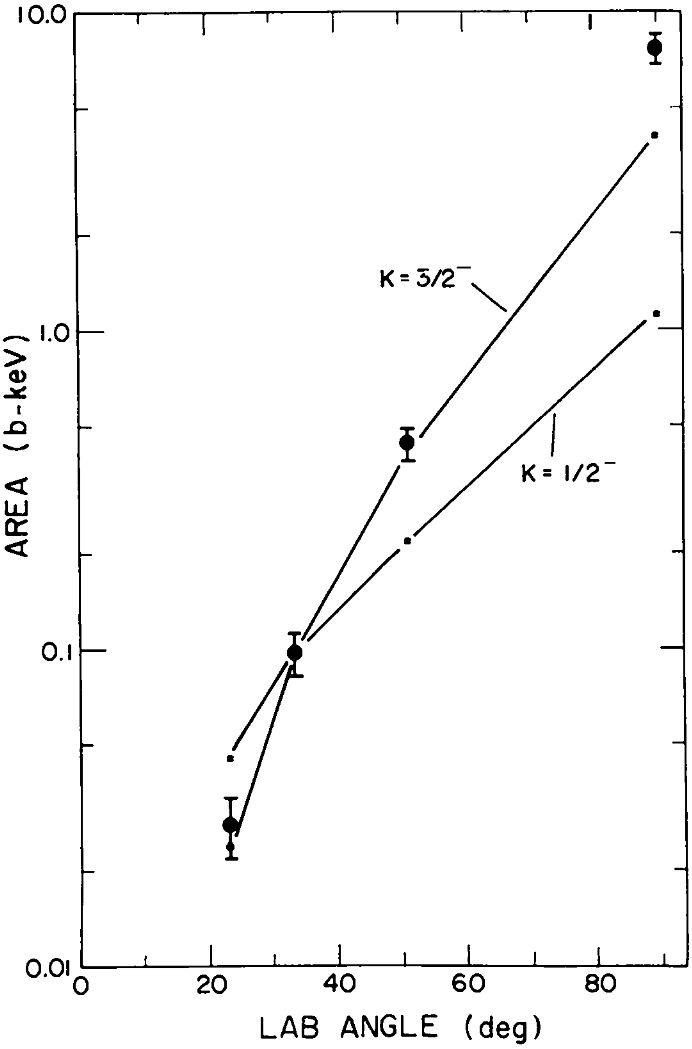

Fig. 13.
Comparison of the experimental areas with theoretical predictions of complete rotational bands for the 1.6-MeV structure. The solid lines connect the theoretical areas for a K = 1/2⁻ band and a K = 3/2⁻ band. Both curves are normalized to the experimental area at θ_m = 33.7°. The predictions for the positive parity bands are similar.

of the theoretical areas for these two bands more than accounts for all experimental areas, again suggesting smaller values for $T_{f,max}$ and/or Γ_{vib}. Using the 4:1 ratio for the K = 3/2 to K = 1/2 strengths normalized to the experimental area at 33.7°, the approximate relative fission strengths (integrated over polar angle) for the K = 1/2, 3/2, and ≥5/2 bands are in the proportion of 1.0:2.8:0.0.

C. Individual Vibrational-Resonance Area Results

So far, we have tried to explain the observed areas in terms of complete K-bands in which each rotational member has the same $T_{f,max}$ and Γ_{vib} parameters. This is idealistic. It is more likely that the fission barrier parameters of individual states are significantly different from each other, and that not all members of a particular K-band would have sufficient strength to be observed in the data. An analysis in terms of individual resonances

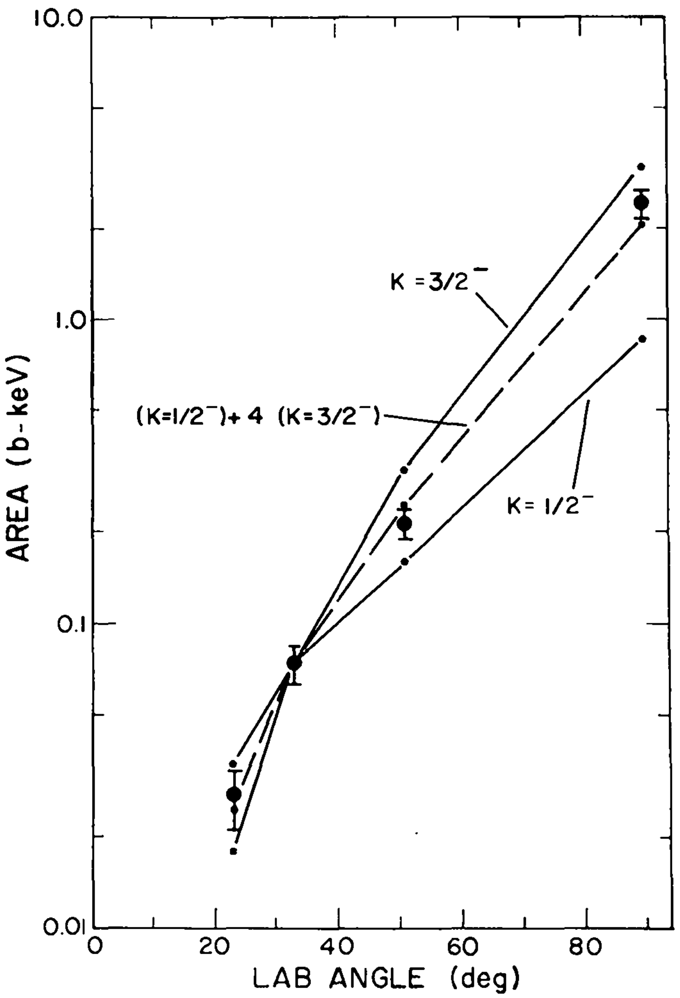

Fig. 14.

Comparison of the experimental areas with theoretical predictions of complete rotational bands for the 1.7-MeV structure. The solid lines connect the theoretical areas for a K = 1/2⁻ band and a K = 3/2⁻ band. The dashed line connects the areas for the combination (K = 1/2⁻) + 4(K = 3/2⁻). All curves are normalized to the experimental area at θ_m = 33.7°. The predictions for the positive parity bands are similar.

with parameters unrelated to each other except in some average sense would be unmanageable without additional data and, therefore, any results would not be very meaningful. It is worthwhile, however, to mention two general observations based on the data in Table V and the experimental areas. Let us concentrate on the 1.6-MeV structure because it is defined better in the gridded data than the other structures. The experimental area of the 30° structure is about 97 mb·keV. An inspection of the K = 3/2 areas in Table V reveals that no single resonance would exhaust this area even if Γ_{vib} is increased to the observed width of ~50 keV; for the 1.6-MeV structure, many K = 3/2 resonances are required. In addition, the K = 3/2 areas would underestimate the experimental 90° area, thus requiring K ≥ 5/2 components. A similar statement can be made for the other two structures, namely, that many individual resonances are required for each structure, and except for possibly the 1.7-MeV structure, K ≥ 5/2 components are present in the structures.

VII. COMPARISON WITH DOUBLE- AND TRIPLE-HUMPED BARRIER CALCULATIONS

Two attempts have been made at a detailed channel analysis of the structure in ^{233}Th in the 1- to 2-MeV neutron energy region using fission cross-section and angular distribution or anisotropy data. Caruana et al.[16] compare the results from a triple-humped model with those from a double-humped model by fitting their angular distribution data and the fission cross-section data of Blons et al.[4] For the double-humped model, they cannot fit both data sets with the same set of K-band parameters, even after an extensive trial-and-error search of many different sets. For the triple-humped model, both data sets in the region of the 1.6- and 1.7-MeV structures can be described adequately by either (1) the set $K = 1/2^+, 5/2^-$ (1.4 MeV), $3/2^+, 3/2^-, 3/2^-, 5/2^-$ (1.6 MeV), and $1/2^+, 5/2^+$ (1.7 MeV), or (2) the set $K = 3/2^+, 1/2^+$ (1.4 MeV), $5/2^-, 3/2^-, 3/2^-, 5/2^-$ (1.6 MeV), and $5/2^+, 1/2^+$ (1.7 MeV). The energy in parentheses indicates the structures to which the preceding K-bands apply. However, neither triple-humped set gives a satisfactory fit to the 1.4-MeV region, although set (2), which has $K = 3/2$ and $1/2$ components, gives a better fit to their 1.35-MeV angular distribution. In general, set (2) agrees better than set (1) with our results, although we require $K = 3/2$ components for the 1.7-MeV structure and, most certainly, $K \geq 5/2$ components for the 1.4-MeV structure.

A significantly better fit to the fission cross section and to all I(0°)/I(90°) data is obtained by Abou Yehia et al.[26] for a double-humped model with the transition states listed in Table VII. The values of Γ_{vib} and $T_{\mathrm{f,max}}$ are calculated from their barrier parameters using Eq. (22a-d). If we assume that our values of σ_{f} are about the same as those used in the analysis in Ref. 26, and that $T_N + T_\gamma \gg T_f$ [consequently their areas are equal to our areas (Tables V and VI) multiplied by $\Gamma_{\mathrm{vib}} \times T_{\mathrm{f,max}}/10$], then their predictions about the relative strengths of the K-bands are in remarkable agreement with our results, particularly for the 1.7-MeV structure. Their ratio of $(K = 3/2):(K = 1/2)$ for the 1.7-MeV structure is 3.6, and we estimated about 4. For the 1.4-MeV structure, their values for $\Gamma_{\mathrm{vib}} \times T_{\mathrm{f,max}}$ give 1.95 for the ratio $(K = 3/2):(K = 1/2)$. This is the source of the factor of 2 for the dashed line in Fig. 12. And, for the 1.6-MeV structure, their parameters support our conclusion that very little $K = 1/2$ component is required to account for the areas at all angles.

TABLE VII

TRANSITION STATE PARAMETERS ($K\pi$, Γ_{vib}, $T_{\mathrm{f,max}}$) FOR THE STRUCTURES AT ~1.4, ~1.6, AND ~1.7 MeV[a]

Structure (MeV)	$K\pi$	Γ_{vib} (keV)	$T_{\mathrm{f,max}}$
1.4	1/2+	75	0.29
	3/2+	80	0.53
1.6	1/2+	107	0.11
	3/2+	82	0.42
	3/2±	53	0.60
	5/2±	83	0.49
1.7	1/2±	47	0.10
	3/2+	42	0.40

[a] Based on the barrier parameters in Ref. 26.

VIII. SUMMARY

We now know from all analyses what the primary K-components are of the fission strength of the structures at 1.4, 1.6, and 1.7 MeV in ^{233}Th. From our results, we can give the relative strengths of the K-components in each structure. We find the approximate proportion of $K = 1/2$ to $K = 3/2$ to $K \geq 5/2$ strengths in the ratios of 1.7:2.4:1.0, 0.0:2.6:1.0, and 1.0:2.8:0.0 for the structures at 1.4, 1.6, and 1.7 MeV, respectively. Furthermore, if the fine structure has a width of about 10 keV (with a limit of <50 keV) then a great many states are required to account for the area of each structure in the fission cross section.

And finally, because our K-component strengths are derived without assuming a particular shape for the fission barrier, they do not confirm the existence of the shallow mass-asymmetric well predicted by Möller and Nix,[6] even though they are consistent with recent triple-humped barrier calculations.

ACKNOWLEDGMENTS

We thank W. A. Teasdale, J. M. Anaya, and C. E. Ragan for their assistance during the initial phases of the experiment, and J. Craven (ORELA staff) for writing the data-acquisition program and for help with computer-related problems.

REFERENCES

1. D. W. Muir and L. R. Veeser, "Neutron-Induced Fission Cross Sections of ^{230}Th and ^{231}Pa," Proc. 3rd Neutron Cross Sections and Technology, Knoxville, Tennessee, 1971; Vol. 1, pp. 292-298.

2. S. Plattard, G. F. Auchampaugh, N. W. Hill, G. de Saussure, R. B. Perez, and J. A. Harvey, "High-Resolution Fission Cross Section of ^{231}Pa," Proc. Intern. Conf. on Nuclear Cross Sections for Technology, Knoxville, Tennessee, 1979 (1980), 491-495.

3. J. Blons, C. Mazur, D. Paya, M. Ribrag, and H. Weigmann, "Rotational Bands in Asymmetrically Deformed ^{231}Th," Phys. Rev. Lett. 41, 1282-1285 (1978).

4. J. Blons, C. Mazur, and D. Paya, "Evidence for Rotational Bands Near the ^{232}Th (n,f) Fission Threshold," Phys. Rev. Lett. 35, 1749-1751 (1975).

5. P. Möller, "Odd-Multipole Shape Distortions and the Fission Barriers of Elements in the Region $84 < Z < 120$," Nucl. Phys. A192, 529-580 (1972).

6. P. Möller and J. R. Nix, "Potential-Energy Surfaces for Asymmetric Heavy-Ion Reactions," Nucl. Phys. A281, 354-372 (1972).

7. J. Blons, C. Mazur, D. Paya, M. Ribrag, and H. Weigmann, "The Asymmetric Deformation of ^{231}Th and ^{233}Th," Winter College on Nuclear Physics and Reactors, Bormio, Italy, 1980.

8. A. Sobiczewski, S. Bjornholm, and K. Pomorski, "The Moment of Inertia and the Energy Gap of Fission Isomers," Nucl. Phys. A202, 274-288 (1973).

9. H. J. Specht, J. Weber, E. Konechy, and D. Heunemann, "Identification of a Rotational Band in the ^{240}Pu Fission Isomer," Phys. Lett. 41B, 43-46 (1972).

10. H. Backe, L. Richter, D. Habs, V. Metag, J. Pederson, P. Singer, and H. J. Specht, "Spectroscopy in the Second Minimum of the Potential Energy Surface of ^{239}Pu," Phys. Rev. Lett. 42, 490-493 (1979).

11. S. Bjornholm and J. E. Lynn, "The Double-Humped Fission Barrier," Rev. Mod. Phys. 52, 725 (1980).

12. A. Sicre, "Ètude de la Fission de ^{232}Pa Induite Par Neutrons Rapides," Ph.D. Thesis, University of Bordeaux, Report CENBG 7603 (1976).

13. P. E. Vorotnikov, S. M. Dobrovina, G. A. Otroshchenco, and V. A. Shigin, "Angular Distributions of Fission Fragments in the Reactions ^{231}Pa(n,f)," Sov. J. Nucl. Phys. 10, 280-281 (1970).

14. G. D. James, J. E. Lynn, and L. G. Earwaker, "Nuclear Spectroscopy of Highly Deformed ^{231}Th," Nucl. Phys. A189, 225-249 (1972).

15. G. Yuen, G. T. Rizzo, A. N. Behkami, and J. R. Huizenga, "Fragment Angular Distributions of the Neutron-Induced Fission of ^{230}Th," Nucl. Phys. A171, 614-624 (1971).

16. J. Caruana, J. W. Boldeman, and R. L. Walsh, "Fission Fragment Angular Distributions for Neutron Fission of ^{232}Th and Their Interpretation with a Triple-Humped Fission Barrier," Nucl. Phys. A285, 205-216 (1977).

17. S. B. Earmagambetov and G. N. Smirenkin, "Fragment Angular Distribution and Channel Analysis of ^{232}Th Neutron Fission," Sov. J. Nucl. Phys. 11, 646-653 (1970).

18. J. W. Behrens, "Systematics of Neutron-Induced-Fission Cross Sections in the MeV Range," Phys. Rev. Lett. 39, 68-71 (1977).

19. S. Lo Nigro and C. Milone, "Angular Distributions of Fragments from Neutron Induced Fission of Thorium," Nucl. Phys. A96, 617-623 (1967)

20. S. Kahn, R. Harman, and V. Forque, "Energy Distributions of Fission Fragments from Uranium Dioxide Films," Nucl. Sci. Eng. 23, 8-20 (1965).

21. J. A. Wheeler, "Channel Analysis of Fission," in *Fast Neutron Physics, Part II*, J. B. Marion and J. L. Fowler, Eds. (Interscience Publishers, Inc., New York, 1963), Chap. V.S., 2051-2184.

22. R. W. Lamphere, "Fission Cross Section and Fragment Angular Distribution for Fast Neutron-Induced Fission of ^{234}U," Nucl. Phys. 38, 561-589 (1962).

23. A. de Shalit and H. Feshbach, *Theoretical Nuclear Physics Vol. 1: Nuclear Structure* (John Wiley & Sons, Inc., New York, 1978).

24. E. M. Lent, "Response of Multiple Collimator Systems to Extended Sources," Nucl. Instrum. Methods 106, 29-34 (1973).

25. J. E. Simmons and R. L. Henkel, "Angular Distribution of Fragments in Fission Induced by MeV Neutrons," Phys. Rev. 120, 198-210 (1969).

26. H. Abou Yehia, J. Jary, J. Trochon, J. W. Boldemann, and A. R. de L. Musgrove, "What Can Be Learned from the Channel Analysis of the ^{232}Th Neutron Fission Cross Section?" Proc. Intern. Conf. on Nuclear Cross Sections for Technology, Knoxville, Tennessee, 1979.

27. W. Hauser and H. Feshbach, "The Inelastic Scattering of Neutrons," Phys. Rev. 87, 366-373 (1952).

28. P. A. Moldauer, "Unitary Models of Nuclear Resonance Reactions," Phys. Rev. 157, 907-921 (1967).

29. J. E. Lynn, "Systematics for Neutron Reactions of the Actinide Nuclei," Atomic Weapons Research Establishment report AWRE-R7468, Harwell, England (November 1974).

30. "Neutron Cross Sections," S. F. Mughabghab and D. I. Garber, Comps., Brookhaven National Laboratory report BNL-325 (National Technical Information Service, 1973), 3rd Ed., Vol. 1, Resonance Parameters.

31. A. Gilbert and A. G. W. Cameron, "A Composite Nuclear Level Density Formula with Shell Corrections," Can. J. Phys. 43, 1446-1496 (1965).

32. Nuclear Data Sheets 20, 179 (1977).

33. J. D. Cramer and J. R. Nix, "Exact Calculation of the Penetrability Through Two-Peaked Fission Barriers," Phys. Rev. C 2, 1048-1057 (1970).

34. E. V. Gai, A. V. Ignatiuk, N. S. Rabotnov, and G. N. Smirenkin, "Double-Humped Barrier in the Quasi-Classical Approximation," Los Alamos National Laboratory report LA-4386-TR (January 1971), translated by A. Vakar from paper AEA/SM/122/132, International Atomic Energy Agency, Second Symposium on the Physics and Chemistry of Fission Processes, Vienna, July 28-August 1, 1969.

Printed in the United States of America
Available from
National Technical Information Service
US Department of Commerce
5285 Port Royal Road
Springfield, VA 22161

Microfiche $3.50 (A01)

Page Range	Domestic Price	NTIS Price Code	Page Range	Domestic Price	NTIS Price Code	Page Range	Domestic Price	NTIS Price Code	Page Range	Domestic Price	NTIS Price Code
001-025	$ 5.00	A02	151-175	$11.00	A08	301-325	$17.00	A14	451-475	$23.00	A20
026-050	6.00	A03	176-200	12.00	A09	326-350	18.00	A15	476-500	24.00	A21
051-075	7.00	A04	201-225	13.00	A10	351-375	19.00	A16	501-525	25.00	A22
076-100	8.00	A05	226-250	14.00	A11	376-400	20.00	A17	526-550	26.00	A23
101-125	9.00	A06	251-275	15.00	A12	401-425	21.00	A18	551-575	27.00	A24
126-150	10.00	A07	276-300	16.00	A13	426-450	22.00	A19	576-600	28.00	A25
									601-up	†	A99

†Add $1.00 for each additional 25-page increment or portion thereof from 601 pages up.